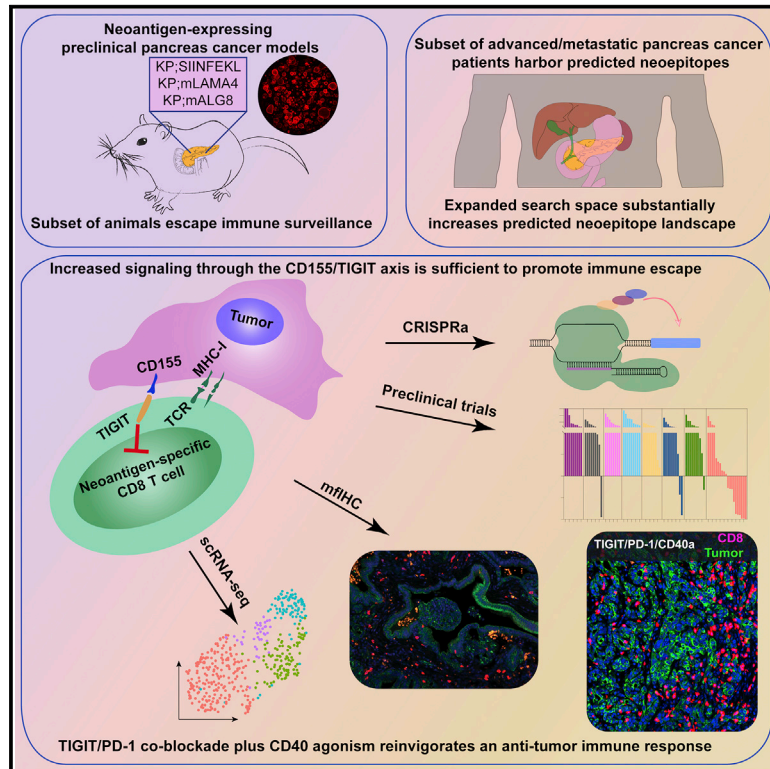


The CD155/TIGIT axis promotes and maintains immune evasion in neoantigen-expressing pancreatic cancer

Graphical abstract



Authors

William A. Freed-Pastor,
Laurens J. Lambert, Zackery A. Ely, ...,
Omer H. Yilmaz, Aviv Regev,
Tyler Jacks

Correspondence

tjacks@mit.edu

In brief

Freed-Pastor et al. identify the CD155/TIGIT axis as a key driver of immune evasion in pancreas cancer. Neoepitope prediction reveals a subset of human pancreas cancer patients with predicted high-affinity neoepitopes and functional interrogation using preclinical models identifies a combination immunotherapy approach (TIGIT/PD-1 co-blockade plus CD40 agonism) capable of eliciting profound anti-tumor responses.

Highlights

- A subset of neoantigen-expressing pancreas cancer evades immune surveillance
- Markers of T cell exhaustion typify pancreas cancer tumor-infiltrating lymphocytes
- The CD155/TIGIT axis promotes immune evasion in pancreas cancer
- TIGIT/PD-1 co-blockade plus CD40 agonism reinvigorates tumor-reactive T cells

Article

The CD155/TIGIT axis promotes and maintains immune evasion in neoantigen-expressing pancreatic cancer

William A. Freed-Pastor,^{1,2} Laurens J. Lambert,^{1,3} Zackery A. Ely,^{1,3} Nimisha B. Pattada,¹ Arjun Bhutkar,¹ George Eng,^{1,4} Kim L. Mercer,¹ Ana P. Garcia,¹ Lin Lin,¹ William M. Rideout III,¹ William L. Hwang,^{1,5,6} Jason M. Schenkel,^{1,7} Alex M. Jaeger,¹ Roderick T. Bronson,¹ Peter M.K. Westcott,¹ Tyler D. Hether,⁸ Prajan Divakar,⁸ Jason W. Reeves,⁸ Vikram Deshpande,⁴ Toni Delorey,⁶ Devan Phillips,⁶ Omer H. Yilmaz,^{1,3,4} Aviv Regev,^{1,3,6,9} and Tyler Jacks^{1,3,10,*}

¹David H. Koch Institute for Integrative Cancer Research, Massachusetts Institute of Technology, Cambridge, MA 02139, USA

²Department of Medical Oncology, Dana-Farber Cancer Institute, Harvard Medical School, Boston, MA, USA

³Department of Biology, Massachusetts Institute of Technology, Cambridge, MA 02139, USA

⁴Department of Pathology, Massachusetts General Hospital, Boston, MA 02114, USA

⁵Department of Radiation Oncology, Massachusetts General Hospital, Harvard Medical School, Boston, MA 02114, USA

⁶Broad Institute of MIT and Harvard, Cambridge, MA 02142, USA

⁷Department of Pathology, Brigham and Women's Hospital, Harvard Medical School, Boston, MA 02115, USA

⁸NanoString Inc., Seattle, WA 98109, USA

⁹Present address: Genentech, 1 DNA Way, South San Francisco, CA, USA

¹⁰Lead contact

*Correspondence: tjacks@mit.edu

<https://doi.org/10.1016/j.ccell.2021.07.007>

SUMMARY

The CD155/TIGIT axis can be co-opted during immune evasion in chronic viral infections and cancer. Pancreatic adenocarcinoma (PDAC) is a highly lethal malignancy, and immune-based strategies to combat this disease have been largely unsuccessful to date. We corroborate prior reports that a substantial portion of PDAC harbors predicted high-affinity MHC class I-restricted neoepitopes and extend these findings to advanced/metastatic disease. Using multiple preclinical models of neoantigen-expressing PDAC, we demonstrate that intratumoral neoantigen-specific CD8⁺ T cells adopt multiple states of dysfunction, resembling those in tumor-infiltrating lymphocytes of PDAC patients. Mechanistically, genetic and/or pharmacologic modulation of the CD155/TIGIT axis was sufficient to promote immune evasion in autochthonous neoantigen-expressing PDAC. Finally, we demonstrate that the CD155/TIGIT axis is critical in maintaining immune evasion in PDAC and uncover a combination immunotherapy (TIGIT/PD-1 co-blockade plus CD40 agonism) that elicits profound anti-tumor responses in preclinical models, now poised for clinical evaluation.

INTRODUCTION

Pancreatic cancer is the third leading cause of cancer-related deaths in the United States (Siegel et al., 2020) and, despite progress in improving chemotherapeutic regimens (Conroy et al., 2011; Von Hoff et al., 2013), metastatic pancreatic adenocarcinoma (PDAC) continues to carry a dismal prognosis. While insights regarding the molecular and cellular mechanisms of immune evasion have fueled tremendous clinical successes in a range of tumor types, microsatellite-stable PDAC, which represents greater than 98% of all patients (Eso et al., 2020), has been largely refractory to available immune checkpoint blockade (O'Reilly et al., 2019). Despite harboring an intermediate mutational burden (Lawrence et al., 2013), recent whole-exome sequencing (WES) efforts have demonstrated that a subset of early-stage PDAC contains predicted neoepitopes (Bailey et al., 2016; Balachandran et al., 2017). In fact, neoantigen-spe-

cific tumor-infiltrating lymphocyte (TIL) clones can be isolated from a subset of PDAC patients (Gros et al., 2019; Parkhurst et al., 2019; Sakellariou-Thompson et al., 2017; Tran et al., 2015). Extensive profiling of the immune landscape in PDAC has uncovered a complex microenvironment, characterized by numerous immune-suppressive cell populations and a subset of patients with exhausted/dysfunctional CD8⁺ T cells, marked by elevated surface expression of the co-inhibitory receptor TIGIT (Liudahl et al., 2021; Steele et al., 2020). However, the tumor reactivity of dysfunctional/exhausted CD8⁺ T cells in PDAC is currently unknown.

Previous work has investigated neoantigen expression in PDAC using transplantation of monolayer cell lines (Evans et al., 2016) or autochthonous genetically engineered mouse models (Hegde et al., 2020). However, the results of these studies have thus far been contradictory, with monolayer-based models leading to preponderant T cell-mediated rejection, while

neoantigen expression paradoxically leads to tumor acceleration in autochthonous PDAC.

Here we demonstrate that PDAC, including advanced/metastatic lesions, harbors predicted high-affinity neoepitopes with novel MHC class I binding ability relative to their wild-type counterparts. Using multiple preclinical models of neoantigen-expressing murine PDAC paired with profiling of human PDAC, we uncover the CD155/TIGIT axis as necessary and sufficient to maintain immune evasion in PDAC. Finally, we reveal a combination immunotherapy (TIGIT/PD-1/CD40a), which leverages this dependency, capable of eliciting profound anti-tumor responses in preclinical models.

RESULTS

Both localized and advanced/metastatic human PDAC harbor predicted high-affinity neoepitopes

Recent sequencing studies have challenged the claim that pancreatic cancer harbors few predicted neoantigens (Bailey et al., 2016; Balachandran et al., 2017). However, these efforts have largely been limited to early-stage/resectable disease, which represents a minority of patients (Ryan et al., 2014), and have primarily focused on missense mutations, which may significantly underestimate the total neoantigen burden in PDAC.

To address the broader neoepitope landscape, we developed a neoepitope prediction pipeline incorporating HLA allele typing, mutation calling, variant effect prediction, and peptide:MHC class I binding predictions; we also expanded the search space to consider variants derived from missense, frameshift, and in-frame insertion/deletion mutations (Figure S1A and STAR Methods). Consistent with prior studies, we uncovered numerous putative neoepitopes in early-stage tumors, profiled as part of The Cancer Genome Atlas (TCGA) (Cancer Genome Atlas Research Network, 2017) (Figure 1A and Table S1). Even after excluding one patient with mismatch repair deficiency, the majority of patients (86%, 127/148) harbored putative neoepitopes, with 73% (108/148) harboring one or more neoepitopes with predicted high-affinity (<50 nM) for MHC class I (Figure 1A). We also examined novel predicted MHC class I binding, in which variants were predicted to confer MHC class I binding (<500 nM) or strong binding (<50 nM) relative to corresponding wild-type sequences predicted to have low-affinity for MHC class I (>1,000 nM) or frameshift-derived variants, which had no corresponding wild-type sequence. Using this “non-binding-to-binding” analysis, 81% (120/148) of patients harbored one or more of these potentially immunogenic neoepitopes (Figure 1B).

To extend these results, we examined advanced/metastatic PDAC patients from the Dana-Farber Cancer Institute (DFCI) PancSeq study (Aguirre et al., 2018), including 57 with matched WES and RNA sequencing (RNA-seq). All (100%, 57/57) of these advanced/metastatic patients harbored predicted neoepitopes, with a sizable proportion (87%; 50/57) possessing predicted high-affinity (<50 nM) neoepitopes (Figure 1C and Table S1). The vast majority (98%; 56/57) harbored one or more “non-binding-to-binding” neoepitopes (Figure 1D). In aggregate, we found that the overall PDAC neoepitope landscape is increased by 28.3% with the inclusion of frameshift and in-frame insertion/deletion mutations (Figures S1B and S1C; Table S1).

Neoantigen-expressing pancreatic organoids model immune clearance and immune evasion

As a subset of both localized and advanced/metastatic PDAC harbors predicted high-affinity MHC class I-restricted neoepitopes, we set out to develop improved preclinical models to delineate the molecular and cellular mechanisms of immune evasion in this subset of patients. Using CRISPR/Cas9-assisted homology-directed repair, we generated knockins using defined neoantigens, expressed from the *Hipp11* safe harbor locus (Hippenmeyer et al., 2010). Specifically, we utilized a high-affinity MHC class I-restricted antigen (OVA_{257–264} [SIINFEKL]), linked on a polycistronic transcript to the red fluorescent protein mScarlet (Bindels et al., 2016), or recently described endogenously arising MHC class I-restricted neoantigens: missense mutations in the laminin α 4 subunit (“LAMA4-G1254V”) or in α -1,3-glucosyltransferase (“ALG8-A506T”) (Alspach et al., 2019; Gubin et al., 2014), fused to the C terminus of mScarlet (Figure 2A). We derived “genetically defined” pancreatic organoids (GDOs) from healthy pancreata of *Kras*^{LSL-G12D^{WT}}; *Trp53*^{fllox/fllox}; *H11*^{neoantigen} (“KP;SIIN;” “KP;mLAMA4;” “KP;mALG8”) animals. Following *ex vivo* delivery of adenoviral Cre recombinase, organoids expressed oncogenic *Kras* with loss of the p53 tumor suppressor gene, in addition to stable and uniform neoantigen expression (Figures 2B and S2A). Orthotopic transplantation of neoantigen-expressing organoids into immune-deficient recipients, using either CD8 T cell depletion or *Rag2*^{−/−} animals, resulted in 100% penetrance of mScarlet-positive (mScarlet⁺) tumor formation (Figure 2C). In contrast, orthotopic transplantation of neoantigen-expressing organoids into immune-competent recipients led to two predominant outcomes: (1) immune-mediated clearance of all neoantigen-expressing tumor cells (no tumor upon necropsy, negative for mScarlet expression [a surrogate for neoantigen expression], termed “non-progressor”) or (2) immune evasion (macroscopic tumor that retained mScarlet expression; termed “progressor”) (Figures 2D, 2E, and S2B). In addition, we observed a subset of immune-competent recipients that retained small areas of mScarlet positivity in the absence of macroscopic tumor formation (termed “intermediate”), potentially reflective of a state of immune equilibrium (Figures 2D, 2E, and S2B). In line with this hypothesis, progressor tumors were significantly smaller than tumors that arose in the absence of an immune-selective pressure, suggestive of a prior state of equilibrium before ultimate immune escape (Figures 2F and S2C). While all three neoantigens evaluated exhibit high-affinity for MHC class I, we were particularly struck by the observation that a substantial portion of tumors harboring the highly immunogenic neoantigen (SIINFEKL) were able to escape immune control while maintaining antigen expression, suggesting that further study of this “progressor” subset could offer insights into the range of immune-evasion mechanisms employed in PDAC.

Flow cytometric profiling demonstrated a range of CD8⁺ T cell infiltration in immune-evasive tumors (Figure S2D), reminiscent of previous profiling efforts in human PDAC (Stromnes et al., 2017). Likewise, histopathologic analysis of immune-evasive tumors revealed both inter- and intra-tumoral heterogeneity, with some areas displaying T cell exclusion, a well-documented phenomenon in PDAC (Joyce and Fearon, 2015; Stromnes et al., 2017), but with other areas displaying robust

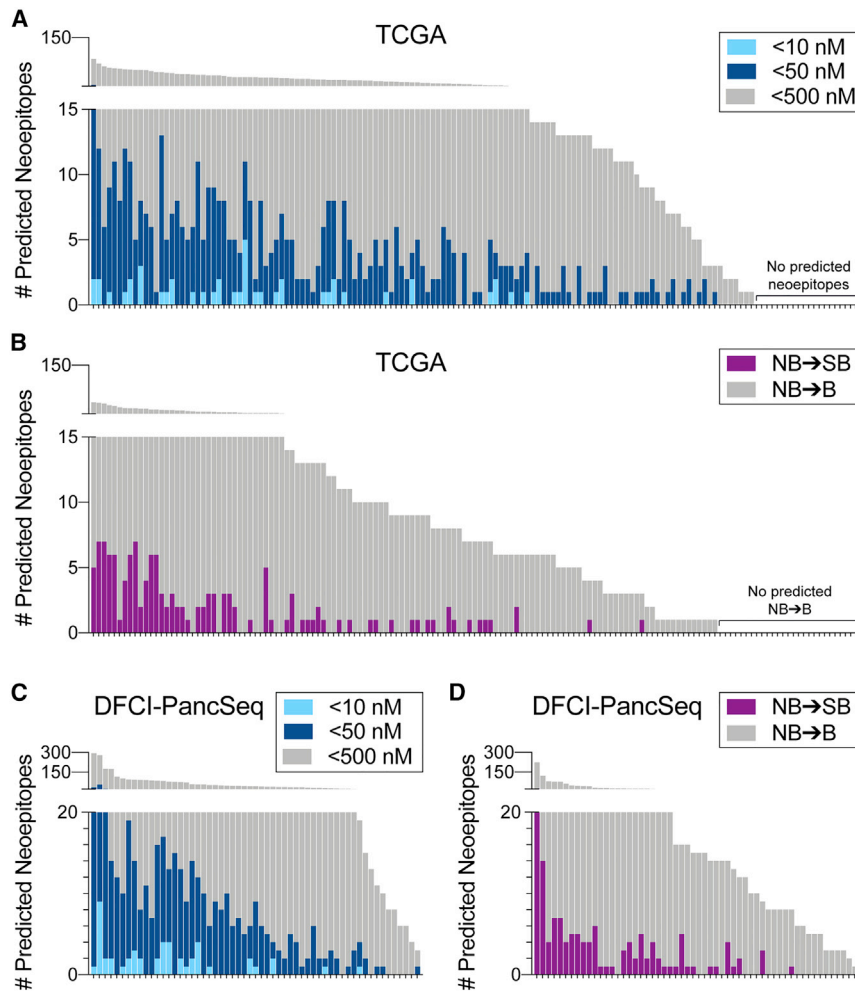


Figure 1. A subset of pancreatic cancer harbors predicted MHC class I-restricted neopeptides

(A and B) Neopeptide landscape in TCGA_PAAD (n = 148) by (A) predicted affinity for MHC class I or (B) predicted non-binder (NB) to binder (B) or strong binder (SB; <50 nM) neopeptides. (C and D) Neopeptide landscape in DFCI-PancSeq (n = 57) by (C) predicted affinity for MHC class I or (D) predicted NB to B or NB to SB neopeptides. See also [Figure S1](#) and [Table S1](#).

We next utilized an organoid/CD8⁺ T cell co-culture system in which immune-evasive (progressor) or immune-deficient KP;SIIN tumor-derived organoids were co-embedded in a three-dimensional extracellular matrix with antigenically stimulated OT-I CD8⁺ T cells (T cell receptor transgenic for SIINFEKL in the context of H-2K^b [[Hogquist et al., 1994](#)]). Both sets of organoids underwent equivalent T cell-dependent killing across multiple E:T ratios ([Figure 2H](#) and [Video S1](#)), definitively demonstrating that organoids derived from immune-evasive tumors retain neoantigen expression and antigen-processing/presentation capacity.

Neoantigen-specific CD8⁺ T cells adopt multiple states of dysfunction in immune-evasive tumors

As we observed evidence of an ongoing CD8⁺ T cell response in immune-evasive tumors, with retained neoantigen expres-

sion, we hypothesized that neoantigen-specific CD8⁺ TILs had become dysfunctional in these tumors. CD8⁺ T cell exhaustion, a state of T cell hypofunctionality ([Blank et al., 2019](#)), has been observed in both murine ([Winograd et al., 2015](#)) and human PDAC ([Liudahl et al., 2021](#); [Steele et al., 2020](#); [Stromnes et al., 2017](#)); however, the (neo)antigen specificity, or even tumor reactivity, of these CD8⁺ TILs has not been firmly established. We utilized flow cytometric profiling to assess T cell exhaustion/dysfunction within the neoantigen-specific compartment (CD44^{hi}Tetramer⁺). We observed no significant differences in the abundance of neoantigen-specific CD8⁺ T cells in progressor versus non-progressor tumors/pancreata ([Figures 3A, S3A, and S3B](#)), but, consistent with the hypothesis that neoantigen-specific CD8⁺ TILs become hypofunctional within immune-evasive tumors, we observed a decrease in their proliferative capacity over time ([Figure 3B](#)). Furthermore, as co-expression of multiple co-inhibitory receptors helps distinguish a dysfunctional phenotype from activation ([Chihara et al., 2018](#); [Schieteringer et al., 2016](#)), we examined co-inhibitory receptor expression (PD-1, TIGIT, TIM-3, LAG-3) on neoantigen-specific TILs and observed a significant accumulation in co-expression of two or more co-inhibitory receptors in immune-evasive tumors ([Figures 3C, S3A, and S3B](#)). We also observed a significant increase in the

CD8⁺ T cell infiltration into tumor nests ([Figures S2E and S2F](#)). Importantly, this inter- and intra-tumoral heterogeneity of T cell infiltration has been recently described in large-scale profiling efforts of the immune contexture in human PDAC ([Liudahl et al., 2021](#); [Steele et al., 2020](#)). These data suggest that immune-evasive neoantigen-expressing tumors with CD8 infiltration must either acquire defects in antigen processing/presentation and/or tumor-reactive T cells must be rendered dysfunctional over time.

To evaluate potential tumor-intrinsic mechanisms of immune escape, we re-isolated organoids from both immune-evasive KP;SIIN tumors and KP;SIIN tumors that arose in immune-deficient animals for *ex vivo* characterization. We performed flow cytometry to characterize neoantigen expression (assessed via mScarlet expression) and surface expression of MHC class I (H-2K^b, H-2D^b) and MHC class II on tumor-derived organoids ([Figures 2G, S2G, and S2H](#)). We observed no loss of neoantigen expression and equivalent basal and induced surface expression of H-2K^b on organoids from immune-evasive tumors compared with organoids from tumors that had never been exposed to an immune-selective pressure ([Figure 2G](#)), suggesting that loss of neoantigen or MHC class I surface expression was not a driving factor in the observed immune evasion.

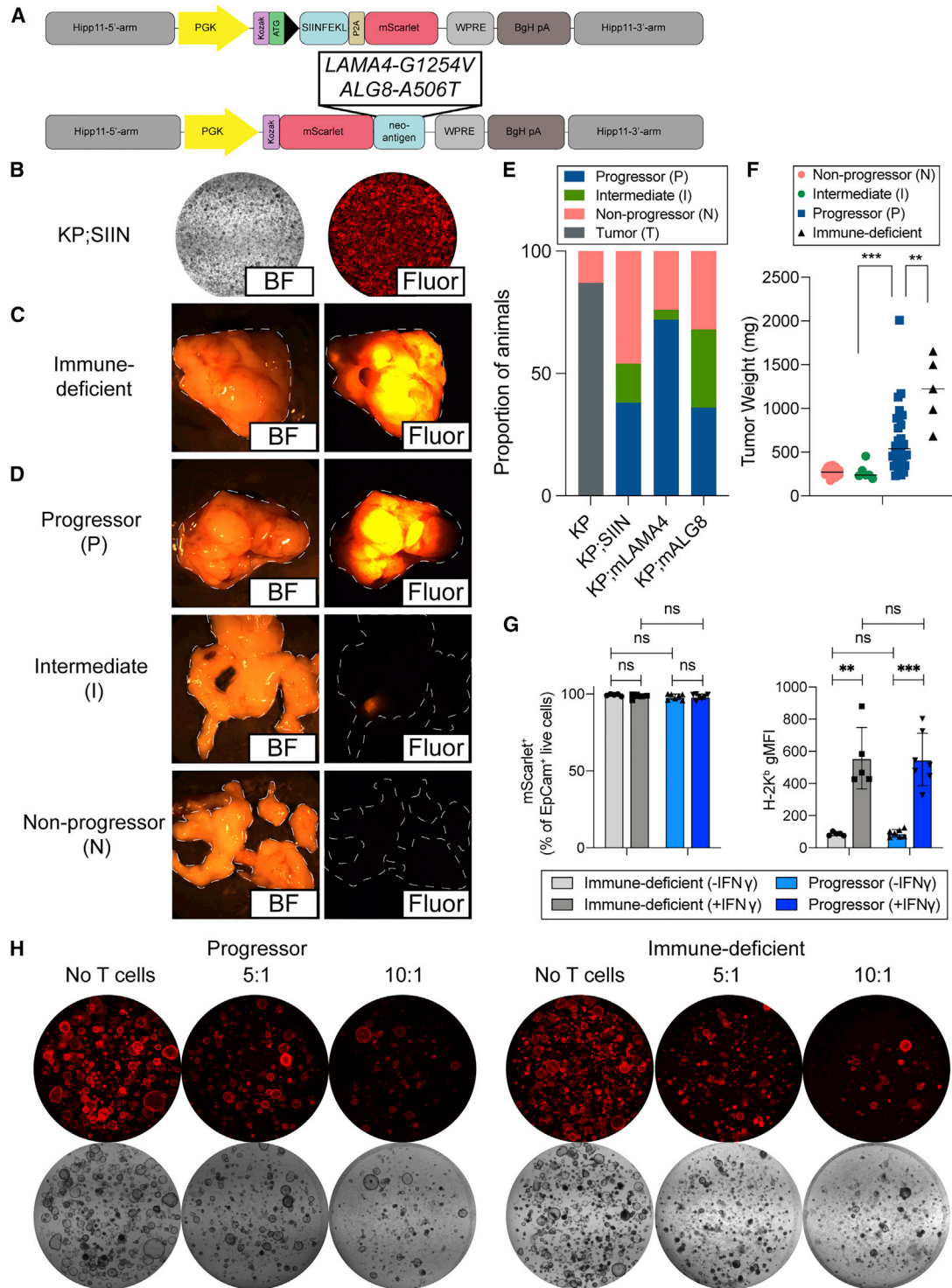


Figure 2. Neoantigen-expressing pancreatic organoids model immune clearance and immune evasion in the same tissue and antigenic context

(A) “H11-SIIN” (top) and “H11-mLAMA4” or “H11-mALG8” (bottom) genomic loci.

(B) Bright-field (left) and fluorescent (right) images of KP;SIIN pancreatic organoids.

(C and D) Bright-field (left) and fluorescence stereomicroscopic (right) images of 8-week tumors following orthotopic transplantation of neoantigen-expressing pancreatic organoids into (C) immune-deficient or (D) immune-competent animals.

(E) Proportion of outcomes at 5 weeks post orthotopic transplantation (KP [n = 15]; KP;SIIN [n = 45]; KP;mLAMA4 [n = 25]; KP;mALG8 [n = 25]).

(legend continued on next page)

co-expression of inhibitory receptors PD1⁺TIGIT⁺, PD1⁺TIM3⁺, and PD1⁺LAG3⁺ in intermediate animals (Figure S3B), suggesting that the acquisition of a hypofunctional phenotype may precede frank immune escape. To further investigate T cell dysfunction in these tumors, we examined terminally exhausted (TIM3⁺TCF1^{lo}) (Miller et al., 2019) neoantigen-specific TILs, which were enriched exclusively in immune-evasive tumors (Figure S3B). Additionally, we observed a minor population of PD1⁺TCF1^{hi} “progenitor-like” (Miller et al., 2019; Sade-Feldman et al., 2018; Siddiqui et al., 2019) neoantigen-specific TILs (Figures S3A and S3B), suggesting that a subset of neoantigen-specific TILs within immune-evasive tumors may retain potential for re-invigoration. To extend these observations beyond the SIINFEKL antigen, we performed flow cytometric immunophenotyping on neoantigen-specific CD8⁺ TILs from immune-evasive KP;SIIN, KP;mLAMA4, and KP;mALG8 tumors. We observed similar patterns of T cell exhaustion within the neoantigen-specific CD8⁺ TIL compartment in all three neoantigen-expressing models (Figure 3D).

To further elucidate potential mechanisms of immune evasion, we performed single-cell RNA-seq (scRNA-seq) (Zheng et al., 2017) on intratumoral neoantigen-specific CD8⁺ T cells sorted from immune-evasive KP;SIIN tumors. After quality control filtering, we retained 447 neoantigen-specific TILs, clustered them into four distinct clusters, and identified genes that were differentially expressed between cells in the four clusters (Figures 3E and 3F; Table S2). Consistent with flow cytometric characterization, cells in the largest cluster (cluster 0) had higher expression of genes associated with CD8⁺ T cell exhaustion (*Pdcd1*, *Havcr2*, *Lag3*, *Tox*) (Figure 3F). We then scored the cells for gene modules derived from mouse CD8⁺ T cells in defined cell states from acute and chronic lymphocytic choriomeningitis virus (LCMV) (Doering et al., 2012). In line with our earlier observations, cluster 0 was enriched for “T cell exhaustion” (CM1), but intriguingly was also enriched for a “chronic effector” signature (CM2) (Figure 3G). Cells in two smaller clusters (clusters 1 and 2) showed higher expression of naive/memory markers (*Sell*, *Ccr7*, *Klf2*, *Tcf7*), potentially reflecting one or more aberrant memory-like cell states, and those in another small cluster (cluster 3) had higher expression of inhibitory Ly49 receptors (*Klra6*, *Klra7*) (Figure 3F), thought to mark a subset of CD8⁺ T regulatory cells previously described in autoimmunity (Kim et al., 2011; Saligramma et al., 2019) and cancer (Singer et al., 2016). Pathway and Gene Set Overdispersion Analysis (PAGODA) (Fan et al., 2016) derived three *de novo* gene set signatures from our scRNA-seq data that overlaid clusters 1 and 2 (Pagoda30) and cluster 0 (Pagoda36, Pagoda45) (Figure 3H and Table S2), further highlighting the heterogeneity within the neoantigen-specific CD8⁺ TIL compartment.

We next compared CD44^{hi}Tetramer⁺ (neoantigen-specific) with CD44^{hi}Tetramer^{neg} (NOT SIINFEKL-specific) CD8⁺ TILs by flow cytometry. As expected, we observed that the

CD44^{hi}Tetramer⁺ subset exhibited a significantly higher proportion of dysfunctional/exhausted TILs (Figure S3C), but intriguingly noted that a portion of CD44^{hi}Tetramer^{neg} CD8⁺ TILs also exhibit marks of T cell dysfunction/exhaustion. This may reflect non-SIINFEKL tumor reactivity (tumor-associated antigen or non-SIINFEKL neoantigen) or potential bystander effects. We noted that TIGIT⁺PD1⁺ co-positivity best differentiated the neoantigen-specific compartment in these analyses, suggesting that these immune axes may play an outsized role in T cell dysfunction in this disease context.

Human PDAC harbors analogous populations of exhausted intratumoral CD8⁺ T cells

To investigate whether these observations could be extended to human PDAC, we isolated intratumoral CD8⁺ T cells from freshly resected surgical samples for flow cytometric profiling. Of 13 specimens evaluated, nine had sufficient CD8⁺ TILs for further immunophenotyping (range 202–17,895 live CD8⁺ TILs). In line with previous reports (Stromnes et al., 2017), the majority (67%–99%) of CD8⁺ TILs were CD45RO⁺ (Figure 4A), reflective of prior antigen experience, with a substantial portion of intratumoral CD8⁺ T cells co-expressing multiple co-inhibitory receptors (PD1⁺TIGIT⁺, PD1⁺LAG3⁺, PD1⁺TIM3⁺, TIGIT⁺TIM3⁺) (Figures 4B and S4A), consistent with our preclinical profiling. In line with our murine models, we observed terminally exhausted (TIM3⁺TCF1^{lo}) CD8⁺ TILs in the majority of tumors (Figure 4C). Progenitor-like (PD1⁺TCF1^{hi}) CD8⁺ TILs have been demonstrated to underlie the proliferative burst in response to PD-1 blockade (Miller et al., 2019; Siddiqui et al., 2019). We observed PD1⁺TCF1^{hi} CD8⁺ PDAC TILs in the majority of tumors, but these represented a small subset of CD8⁺ TILs (Figure 4D), potentially in line with the observed lack of clinical benefit using PD-(L)1 blockade as monotherapy in PDAC (Brahmer et al., 2012; O'Reilly et al., 2019). However, we also observed a population of HLA-DR⁺Ki67⁺CD57^{neg} CD8⁺ TILs in the majority of tumors (Figure 4E), suggesting that there are recently activated, proliferating, and non-senescent intratumoral CD8⁺ T cells in PDAC with potential for therapeutic re-invigoration.

We next investigated T cell phenotypes in previously reported scRNA-seq of human PDAC patients (n = 24) (Peng et al., 2019) (Figures 4F, S4B, and S4C). We computationally “sorted” CD3⁺CD8⁺ and CD3⁺CD4⁺ cells and examined the expression in these selected cells of T cell exhaustion-associated genes (encoding PD-1, TIGIT, TIM-3) and expression of gene signatures derived from murine neoantigen-specific TILs (Figures 4F and 4G). All three gene signatures from murine neoantigen-specific TIL profiling were expressed in specific subsets of CD8⁺ TILs in human PDAC (Figure 4G). Collectively, these data suggest that neoantigen-specific TILs from murine immune-evasive PDAC reflect a subset of CD8⁺ TILs in human PDAC, suggesting that these preclinical models accurately recapitulate a subset of human disease.

(F) Tumor/pancreas weights 8–10 weeks post orthotopic transplantation of KP;SIIN pancreatic organoids (n = 5 “immune-deficient;” n = 24 “N;” n = 6 “I;” n = 30 “P;” bar represents median).

(G) Flow cytometry of mScarlet (left) or surface MHC-I [H-2K^b] (right) on tumor-derived organoids from progressor (n = 7) or immune-deficient (n = 5) animals ± interferon-γ (mean ± SD).

(H) Representative images of organoid/CD8 T cell co-culture with indicated E:T ratios.

Statistical analyses in (F) and (G): two-sided Mann-Whitney U test (ns, non-significant; **p < 0.01; ***p < 0.001). See also Figure S2.

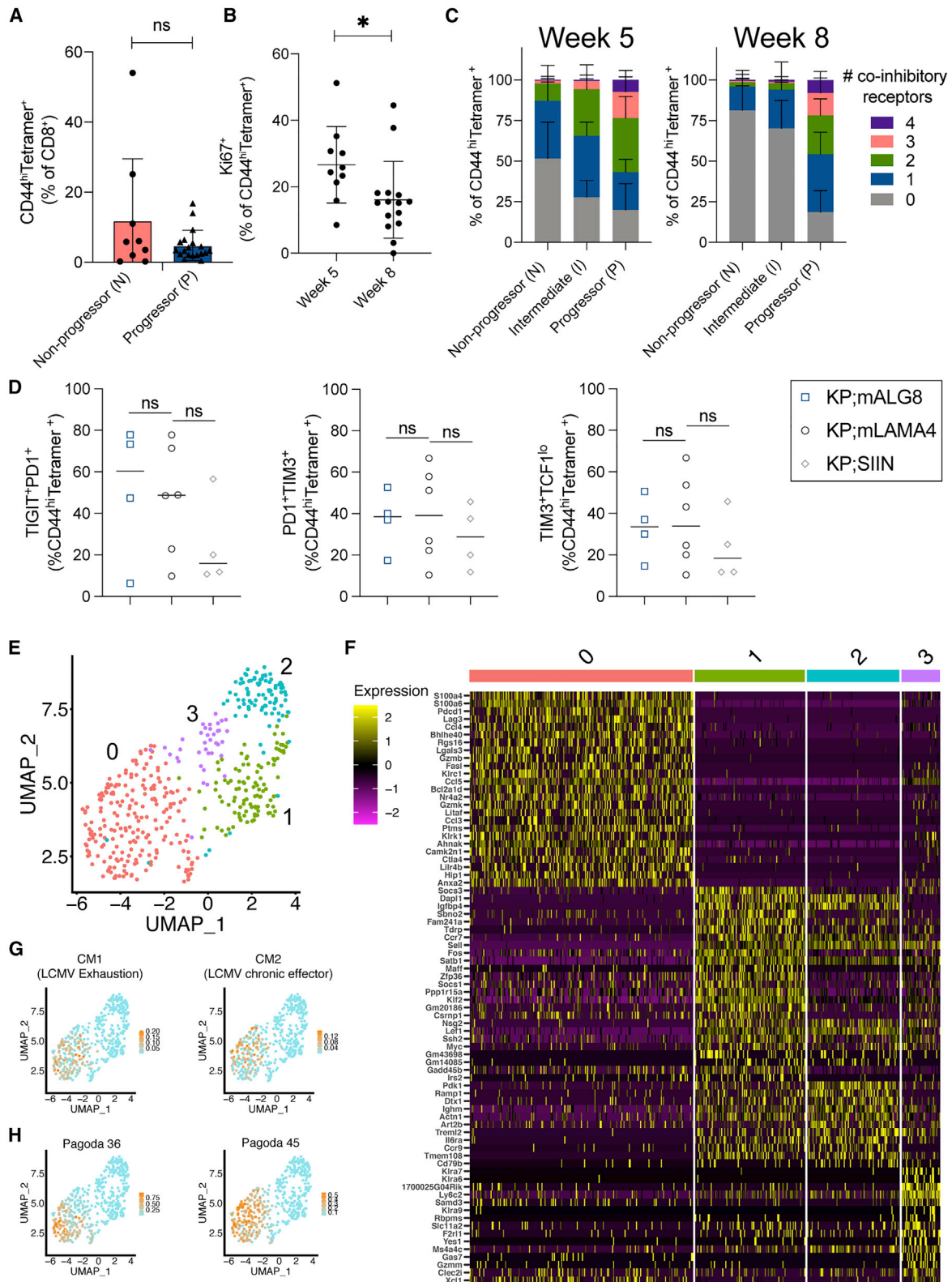


Figure 3. T cell exhaustion typifies the neoantigen-specific TIL response in immune-evasive PDAC

(A) Flow cytometry of neoantigen-specific (CD44^{hi}Tetramer⁺) CD8⁺ T cells in tumors/pancreata at 9–10 weeks post initiation (mean ± SD).

(B) Ki67⁺ of CD44^{hi}Tetramer⁺CD8⁺ TILs from progressor tumors (mean ± SD).

(C) Inhibitory receptor (PD-1, TIGIT, TIM-3, LAG-3) co-positivity as indicated by color in CD44^{hi}Tetramer⁺CD8⁺ TILs from KP;SIIN tumors/pancreata (mean ± SD).

(legend continued on next page)

Elevated expression of CD155 in murine and human PDAC

Given the enrichment of neoantigen-specific T cell exhaustion/dysfunction in murine immune-evasive tumors and the presence of analogous populations in human PDAC, we next examined inhibitory ligand expression. We evaluated PD-L1 (a ligand for PD-1), Galectin 9 (a ligand for TIM-3), and CD155 (a ligand for TIGIT) using immunohistochemical analysis of murine immune-evasive PDAC tissue microarrays (TMAs). While we detected occasional PD-L1 and/or Galectin 9 positivity, the vast majority of tumor cells was negative or expressed low levels of these inhibitory ligands (Figure S5A). This is consistent with prior reports (Stromnes et al., 2017; Yarchoan et al., 2019) that have shown human PDAC to be largely devoid of PD-L1. In contrast, elevated CD155 expression was observed in a substantial fraction of murine immune-evasive tumors (Figures 5A and S5A) and human PDAC (Figure 5B). We computed H-scores (Hirsch et al., 2003) for CD155 in both murine and human PDAC and found that CD155 expression was significantly higher in tumor samples compared with healthy pancreas controls (Figures 5A and 5B), although it is important to point out that approximately 20% of human tumors showed no CD155 expression. While we observed elevated CD155 expression, we cannot rule out the contribution of additional inhibitory ligands that were not directly assessed in this analysis.

To assess expression specifically within the malignant compartment, we utilized murine tumor-derived organoids and human PDAC patient-derived organoids. We observed elevated surface expression of CD155 on both human (Figure S5B) and murine (Figure 5C) tumor-derived organoids. In contrast, we observed low basal expression of surface PD-L1 on murine tumor-derived organoids (Figure 5D), although PD-L1 surface expression could be induced with interferon- γ (Figure S5C). We observed elevated CD155 on organoids isolated from immune-evasive tumors as well as organoids derived from tumors never exposed to an immune-selective pressure, suggesting that CD155 upregulation may be a frequent feature of pancreatic tumorigenesis that is co-opted for immune evasion rather than an acquired feature during immune escape.

To investigate the impact of genetic driver events on CD155 expression, we derived an allelic series of isogenic murine GDOs: wild-type (WT), *Kras*^{LSLG12D/+} (K), *Trp53*^{fllox/fllox} (P), and *Kras*^{LSLG12D/+}*Trp53*^{fllox/fllox} (KP). We observed that surface CD155 expression was unchanged upon expression of either oncogenic *Kras* or loss of p53 alone but was significantly increased in the presence of concomitant oncogenic *Kras* expression and p53 loss (Figure 5C), suggesting a possible interplay between these canonical PDAC-associated oncogenic events leading to upregulation of CD155 expression.

To extend this observation, we assessed mRNA expression of *PVR* (encoding CD155), *CD274* (encoding PD-L1), *PVRL2* (encoding CD112), *PDCD1LG2* (encoding PD-L2), and *LGALS9*

(encoding Galectin 9) within PDAC patient samples from TCGA, stratified on the basis of *KRAS* and/or *TP53* mutational status. In line with observations in murine PDAC, we observed significantly elevated expression of CD155 (*PVR*) in PDAC harboring both oncogenic *KRAS* and *TP53* mutations/loss (“KP”) compared with samples that were wild-type for either of these genes (“non-KP”) (Figure 5E). We did not observe significant differences in other inhibitory ligand expression between these patient cohorts (Figure S5D). Of note, given the near universal presence of *KRAS* mutations in PDAC, we were unable to isolate the effects of *KRAS* mutation from *TP53* mutation/loss in this disease context. To evaluate whether a similar paradigm extends beyond PDAC and to attempt to isolate the effects of each oncogenic event, we stratified TCGA datasets from lung (LUAD) and colon (COAD) adenocarcinoma based on *KRAS* and/or *TP53* mutational status. While in lung adenocarcinoma mutation of either *KRAS* or *TP53* alone were associated with elevated expression of CD155 (*PVR*) (Figure S5E), only the combination of oncogenic *KRAS* and *TP53* mutation/loss (KP) was associated with elevated CD155 (*PVR*) expression in colon cancer (Figure 5F), highlighting potential tissue-specific differences in CD155 (*PVR*) regulation.

To further investigate the role of the CD155/TIGIT axis in human PDAC immune evasion, we leveraged our neopeptide predictions (Figure 1) to stratify patients by overall neopeptide burden (<500 nM) and then queried CD155 expression. Tumors with a high burden (top 25%) of predicted neopeptides exhibited on average a significantly elevated CD155 expression compared with tumors with a low burden (bottom 25%) (Figure 5G). Likewise, as our earlier analyses suggested that a substantial portion of PDAC harbors neopeptides with high-affinity for MHC class I (<50 nM) or that acquire the ability to bind to MHC class I (“non-binding-to-binding”), characteristics which correlate with increased immunogenic potential (Wells et al., 2020), we queried whether a higher burden of neopeptides within these classes also associates with CD155 expression. We observed significantly elevated CD155 expression in patients with more “non-binding to binding” neopeptides (Figure S5F) and in patients with predicted high-affinity neopeptides (Figure S5G), suggesting a potential functional role for the CD155/TIGIT axis in mediating immune evasion in human pancreatic cancer.

Preclinical activity of TIGIT/PD-1/CD40a combination immunotherapy in neoantigen-expressing PDAC

Next, we set out to investigate the relevance of the CD155/TIGIT axis in a therapeutic context. As T cell dysfunction is associated with both chronic antigen stimulation and suboptimal co-stimulation (Wherry and Kurachi, 2015), we reasoned that the combination of CD40 agonism plus rationally guided immune checkpoint blockade (ICB) might be able to overcome T cell dysfunction in these tumors. CD40 is expressed on the surface of antigen-presenting cells (APCs) and is crucial for mediating

(D) Flow cytometric characterization of neoantigen-specific (CD44^{hi}Tetramer⁺) TILs at 5 weeks post initiation (bar represents median).

(E) Uniform manifold approximation and projection (UMAP) of scRNA-seq of neoantigen-specific (CD8⁺CD44^{hi}Tetramer⁺) TILs from immune-evasive tumors.

(F) Heatmap of differentially expressed genes between clusters with selected genes highlighted.

(G and H) UMAPs overlaid with (G) gene module expression for “LCMV T cell exhaustion” (CM1) and “LCMV T cell chronic effector” (CM2) or (H) indicated PAGODA gene expression programs.

Statistical analyses in (A), (B), and (D): two-sided Mann-Whitney U test (ns, non-significant; *p < 0.05). See also Figure S3 and Table S2.

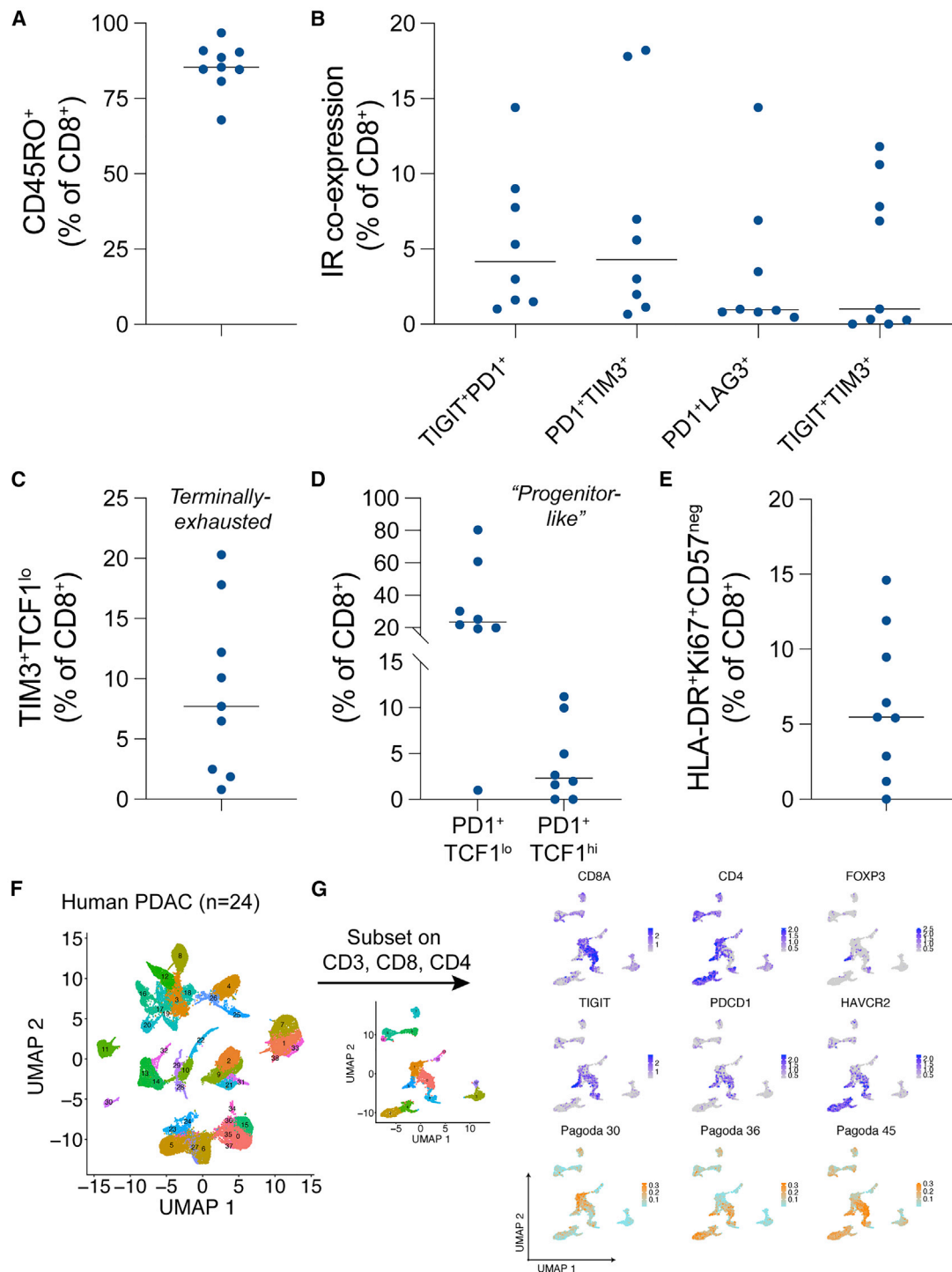


Figure 4. Human PDAC harbors exhausted CD8⁺ TILs

(A–E) Flow cytometric profiling of human PDAC CD8⁺ TILs for: (A) CD45RO; (B) inhibitory receptor (TIGIT, PD-1, TIM-3, LAG-3) co-expression; (C) TIM3⁺TCF1^{lo}; (D) PD-1⁺TCF1^{lo} and PD-1⁺TCF1^{hi}; or (E) HLA-DR⁺Ki67⁺CD57^{neg}. Bars represent median.

(F) UMAP of human PDAC scRNA-seq data (n = 24 patients) (Peng et al., 2019).

(G) Computationally sorted cell subsets and UMAPs overlaid with indicated genes/signatures.

See also Figure S4.

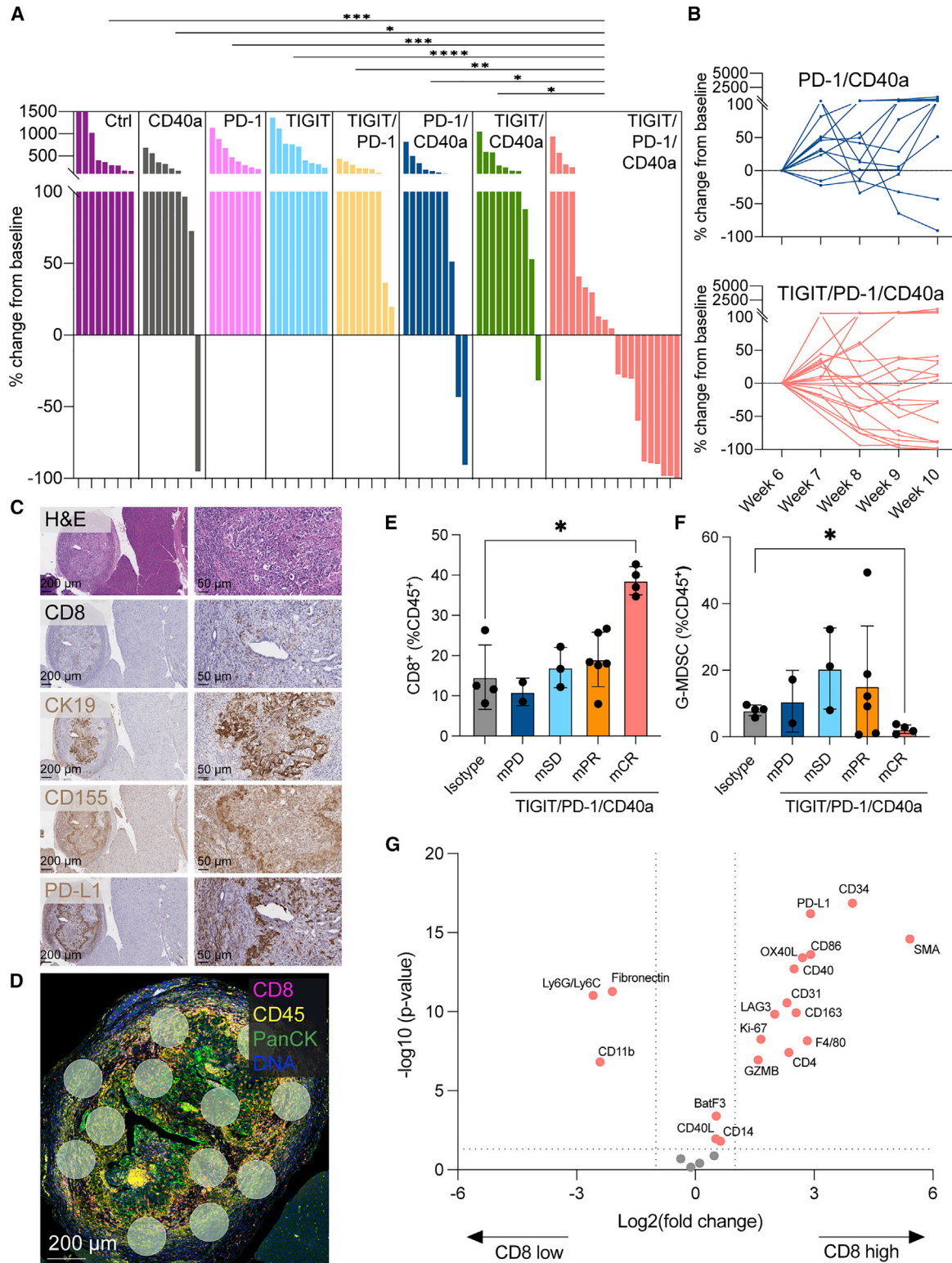


Figure 6. TIGIT/PD-1/CD40a combination immunotherapy elicits anti-tumor responses in immune-evasive PDAC

(A) Waterfall plot of evaluable tumors at 4 weeks of treatment.

(B) Spider plots of treatment response to PD-1/CD40a (top) and TIGIT/PD-1/CD40a (bottom).

(C) Representative staining of CD8 α , cytokeratin 19 (CK19), CD155, and PD-L1 of responders following 4 weeks of TIGIT/PD-1/CD40a.

(legend continued on next page)

crosstalk between APCs and T cells (Johnson et al., 2017; Vonderheide, 2018). Agonistic CD40 antibodies bypass the need for CD4⁺ T cell help (Ribas et al., 2001) and can enhance anti-tumor responses with ICB (Byrne and Vonderheide, 2016; Ma et al., 2019; Vonderheide, 2020; Winograd et al., 2015). Importantly, the PD-1/PD-L1 and TIGIT/CD155 axes coordinately function to dampen a productive CD8⁺ T cell response, and co-blockade has demonstrated synergy in preclinical models and in early-stage clinical trials (Anderson et al., 2016; Hung et al., 2018; Rodriguez-Abreu et al., 2020).

Following orthotopic transplantation of KP;SIIN organoids into immune-competent animals and confirmation of tumor establishment, animals were randomized by baseline tumor volume to receive mono- or dual-ICB, in the presence or absence of CD40 agonism, at 6 weeks post initiation. Specifically, animals were allocated to an isotype control arm or therapeutic arms (CD40 agonist [CD40a], anti-PD-1, anti-TIGIT, anti-TIGIT/PD-1, anti-PD-1 + CD40a, anti-TIGIT + CD40a, anti-TIGIT + anti-PD-1 + CD40a) for treatment over 4 weeks, and tumors were longitudinally evaluated via high-resolution ultrasound imaging. Tumor response was determined using modified RECIST criteria (Gao et al., 2015), previously validated for volumetric tumor response in preclinical models. As expected, isotype control-treated tumors grew unabated with 0% objective response rate (ORR) and 0% disease control rate (DCR) (n = 15, Figures 6A and S6A). Consistent with clinical observations, mono- or dual-ICB (PD-1, TIGIT, PD-1/TIGIT) exhibited no tumor responses (0% ORR/DCR for monotherapy; 0% ORR and 22% DCR with TIGIT/PD-1 co-blockade [n = 9–10 per arm], Figures 6A and S6A). CD40a monotherapy resulted in an 11% ORR and 33% DCR (n = 9, Figures 6A and S6A), but the majority of animals quickly progressed through monotherapy. When CD40a was combined with either PD-1 blockade or TIGIT blockade, we observed primarily disease stabilization with few tumor responses (9% ORR, 54% DCR with PD-1/CD40a; 0% ORR, 18% DCR with TIGIT/CD40a [n = 11 per arm], Figures 6A, 6B, and S6A), potentially consistent with the early clinical promise of CD40a/PD-1 combinations currently being evaluated in clinical trials (O'Hara et al., 2021). In contrast to all other combinations investigated, TIGIT/PD-1 co-blockade plus CD40 agonism (TIGIT/PD-1/CD40a) produced significant tumor responses (46% ORR, 71% DCR) with 23% complete responses (mCR) (n = 48, Figures 6A and 6B). These data support the hypothesis that combinatorial strategies to simultaneously boost and reinvigorate an anti-tumor immune response are needed to overcome the profoundly immunosuppressive PDAC microenvironment and, furthermore, that TIGIT blockade may overcome pre-existing or acquired resistance to CD40a/PD-1 therapy. As TIGIT blockade has already demonstrated safety/tolerability in human patients, with hints of efficacy in other tumor types

(Harjunpää and Guillerey, 2020; Rodriguez-Abreu et al., 2020; Schnell et al., 2020), and combination CD40 agonism + PD-1 blockade has shown safety and early clinical promise in PDAC (Vonderheide, 2020; O'Hara et al., 2021), TIGIT/PD-1/CD40a is poised for rapid clinical evaluation.

To investigate mechanisms of effectiveness and resistance to TIGIT/PD-1/CD40a combination therapy, we treated animals harboring immune-evasive tumors with TIGIT/PD-1/CD40a as described above. Tumors were tracked using weekly ultrasound imaging to facilitate assignment into responder (partial [mPR] or complete [mCR] responses), stable disease (mSD), or non-responder (progressive disease [mPD]) categories. Following 28 days of treatment, tumors (or remaining pancreatic tissue in the case of complete response) were harvested for flow cytometric profiling, conventional immunohistochemical analysis, or spatially resolved multiplexed protein profiling using NanoString GeoMx DSP.

We observed abundant intratumoral CD8⁺ T cells in responder animals (Figures 6C and 6D), with a less pronounced CD8⁺ infiltrate with clear areas of T cell exclusion in non-responder animals (Figures S6B–S6D). Immunohistochemical analysis also demonstrated elevated PD-L1 and CD155 within the tumor-adjacent stroma (TAS) and at the tumor-stromal interface (TSI) of responder tumors (Figure 6C), potentially reflecting a mechanism of acquired resistance to CD40 agonism, which may be overcome through TIGIT/PD-1 co-blockade.

To further characterize changes in the immune microenvironment following TIGIT/PD-1/CD40a therapy, we performed flow cytometric immunophenotyping of CD45⁺ cell subsets following 28 days of control or experimental (TIGIT/PD-1/CD40a) therapy. We observed an increase in CD8⁺ T cell infiltration into responder (mCR/mPR) tumors and a concomitant decrease in immunosuppressive myeloid subsets, most strikingly in granulocytic myeloid-derived suppressor cells (G-MDSCs) (Figures 6E and 6F). We also observed a significant decrease in overall myeloid infiltration (CD11b⁺) and monocytic MDSCs, but not in tumor-associated macrophages, following TIGIT/PD-1/CD40a (Figures S6E–S6H).

We next employed NanoString GeoMx DSP, which utilizes oligonucleotide-tagged antibodies containing a photocleavable linker and UV illumination of defined areas of interest, to enable spatially resolved high-plex protein labeling of tumors following TIGIT/PD-1/CD40a therapy. Consistent with our prior analyses, we observed abundant intratumoral CD8⁺ T cells in responder animals, with CD8⁺ T cells largely restricted to the periphery of non-responder tumors. In both responder and non-responder tumors, we observed markers of effector T cell function (Granzyme B) and proliferation (Ki67) in areas of high CD8⁺ T cell infiltration, but observed elevated expression of MDSC markers (CD11b, Ly6G/C) in areas of T cell exclusion uniquely in non-

(D) Representative multiplex fluorescent immunohistochemistry with NanoString GeoMx DSP areas of interest of a responder tumor (mPR) following 4 weeks of TIGIT/PD-1/CD40a.

(E and F) Flow cytometric analysis of (E) CD8⁺ T cells and (F) G-MDSCs (CD45⁺CD11b⁺F4/80^{low}Ly6C^{low}Ly6G^{high}) (mean ± SD).

(G) Differential protein expression in “CD8 high” versus “CD8 low” AOs in non-responder tumors following 4 weeks of TIGIT/PD-1/CD40a. Red: false discovery rate (FDR) < 0.05.

Statistical analyses: two-sided Mann-Whitney U test of percent change at 4 weeks of therapy (A); two-sided Mann-Whitney U test (E and F); linear mixed-effect model with Benjamini-Hochberg FDR (G). ns, non-significant; *p < 0.05; **p < 0.01; ***p < 0.001; ****p < 0.0001.

See also Figure S6.

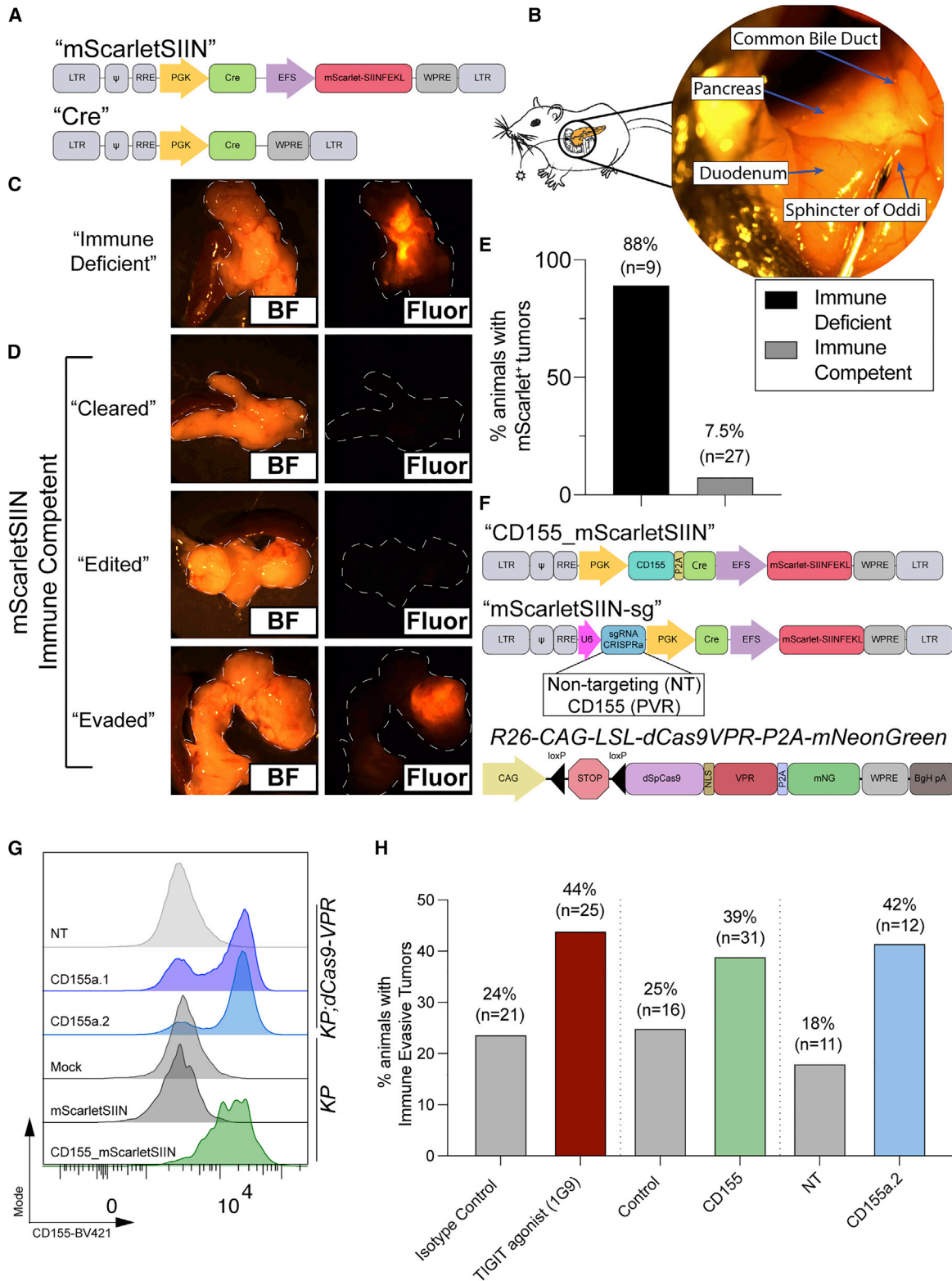


Figure 7. Elevated CD155/TIGIT signaling is sufficient to promote immune evasion in autochthonous PDAC

(A) Lentiviral vectors to generate autochthonous neoantigen-expressing PDAC or control.

(B) Retrograde pancreatic ductal instillation of lentivirus.

(legend continued on next page)

responder tumors (Figures 6G, S6C, and S6D), suggesting a potential role for MDSC-mediated T cell exclusion in resistance to therapy.

Collectively, these data support CD8⁺ T cell re-invigoration as a key marker of response and suggest that T cell exclusion, possibly mediated by G-MDSCs, may be a key driver of resistance. However, future studies will be needed to uncover potential biomarkers in tumors prior to treatment that can be used to select patients most likely to benefit from therapy.

The CD155/TIGIT axis is sufficient to promote immune evasion in PDAC

As an orthogonal approach to our organoid-based preclinical models, we adapted retrograde pancreatic duct delivery (Chiou et al., 2015) to generate a genetically tractable autochthonous mouse model of neoantigen-expressing PDAC. Specifically, we engineered the lentiviral vector used to initiate PDAC in *Kras*^{LSL-G12D/+}; *Trp53*^{fl/fl} (KP) animals to additionally encode a defined neoantigen (“mScarletSIIN;” OVA_{257–264} [SIINFEKL] and OVA_{323–339}) (Figure 7A). Retrograde ductal instillation (Figure 7B) of Cre-expressing lentivirus led to histologically confirmed pancreatic intraepithelial neoplasia (PanIN) and/or PDAC formation in ~90% of immune-deficient or immune-competent animals by 9 weeks post initiation (Figure S7A). To examine the effects of neoantigen expression in autochthonous PDAC, we performed parallel surgeries in immune-competent and immune-deficient (CD8 α -depleted) KP animals. Analogous to Cre expression alone, ~90% of immune-deficient animals transduced with mScarletSIIN developed histologically confirmed PanIN/PDAC by 9 weeks post initiation (Figure S7A). Tumors that developed in the absence of CD8⁺ T cells retained neoantigen expression within PanIN/PDAC lesions (Figures 7C and 7E). In contrast, approximately 50% of immune-competent animals initiated with mScarletSIIN failed to develop tumors by 9 weeks post initiation (Figures 7D, S7B, and S7C), consistent with observations of immune clearance using neoantigen-expressing organoids. However, unlike our organoid-based models, we observed a subset of animals (~40%) that developed macroscopic tumors which failed to maintain mScarlet expression (assessed by both fluorescence stereomicroscopy and immunohistochemical analysis), suggestive of immune editing (Figures 7D and S7D). This difference can likely be attributed to site-specific effects of stochastic lentiviral integration in the autochthonous model, compared with expression from a safe harbor locus in our organoid-based models. Lastly, while less frequent than in our organoid-based model, a reproducible subset (7%–20%) of immune-competent animals initiated with mScarletSIIN developed immune-evasive tumors (Figures 7D, 7E, and S7E). While we observed a robust neoantigen-specific CD8⁺ TIL response in both early- and late-stage lesions (Figures

S7F and 7G), immune-evasive autochthonous tumors harbored intratumoral neoantigen-specific CD8⁺ T cells with co-expression of multiple co-inhibitory receptors (including PD-1⁺TIGIT⁺) (Figure S7G), analogous to observations in our organoid-based models and in human PDAC.

We took advantage of both the relative rarity of immune-evasive tumors and the genetic tractability of this model to evaluate whether genetic or pharmacologic modulation of the CD155/TIGIT axis could promote immune evasion. To investigate the effect of tumor-specific inhibitory ligand expression, we re-engineered the mScarletSIIN lentivirus to additionally express the cDNA for *Pvr* (encoding CD155) (Figure 7F). Using lentiviral transduction of organoids, we confirmed the expected up-regulation of surface CD155 (Figure 7G). As an orthogonal approach, we utilized CRISPR activation (CRISPRa) to upregulate CD155 from the endogenous *Pvr* locus. To facilitate efficient *in vivo* CRISPRa, we generated a knockin allele at the *Rosa26* locus (Soriano, 1999) to enable Cre-mediated conditional expression of dCas9-VPR (Chavez et al., 2015) (Figure 7F). Using lentiviral transduction of KP;dCas9-VPR organoids, we validated two single guide RNAs (sgRNAs) targeting the promoter of *Pvr*, both of which upregulated surface CD155 to similar levels as cDNA expression (Figure 7G). One of the two sgRNAs tested (*Cd155a.2*) consistently led to more uniform upregulation of surface CD155, and thus we opted to proceed with this sgRNA for *in vivo* evaluation.

To evaluate the effects of tumor-restricted inhibitory ligand overexpression in autochthonous neoantigen-expressing PDAC, we randomized KP animals to receive retrograde ductal instillation of control (mScarletSIIN) or CD155-mScarletSIIN lentiviruses. In parallel, KP;dCas9-VPR animals were instilled with mScarletSIIN lentivirus additionally encoding either a non-targeting control sgRNA or *Cd155a.2*. Using either cDNA- or CRISPRa-mediated overexpression, tumor-specific CD155 up-regulation resulted in an increase in the proportion of immune evasion. Specifically, *Pvr* cDNA elicited 39% (n = 31) mScarlet⁺ tumors (an increase from 25% [n = 16] in control animals) and *Cd155a.2* CRISPRa led to 42% (n = 12) immune evasion (an increase from 18% [n = 11] in control animals) (Figure 7H), suggesting that forced elevation of CD155 promotes immune evasion in PDAC.

Finally, to assay the effect of elevated TIGIT activity, we initiated autochthonous PDAC in KP animals using mScarletSIIN and randomized animals immediately following pancreatic duct surgery to receive a TIGIT agonistic antibody (clone 1G9) (Dixon et al., 2018) or an isotype control antibody. In line with our observations modulating CD155, 44% (n = 25) of animals in the TIGIT agonist arm exhibited immune evasion, compared with 24% (n = 21) of isotype control-treated animals (Figure 7H). While no approach was as effective as complete CD8 depletion,

(C and D) Bright-field (left) and fluorescence stereomicroscopic (right) images of representative 9-week autochthonous tumors generated using mScarletSIIN in (C) CD8 α -depleted or (D) immune-competent animals.

(E) Proportion of animals with mScarlet positivity as assessed by fluorescence stereomicroscopy, 9 weeks post initiation.

(F) Lentiviral vectors and R26-dCas9-VPR knockin allele used to modulate CD155 (*Pvr*) expression in autochthonous PDAC.

(G) Flow cytometric assessment of surface CD155 on pancreatic organoids following transduction with indicated lentiviruses.

(H) Proportion of animals with mScarlet positivity by fluorescence stereomicroscopy at 9–12 weeks post initiation following indicated genetic or pharmacologic modulation.

See also Figure S7.

collectively these data reinforce the functional importance of the CD155/TIGIT axis in PDAC immune evasion.

DISCUSSION

Neoantigen-specific CD8⁺ T lymphocytes, which recognize cognate antigen presented in the context of MHC class I, are thought to underlie the success of current immune-based strategies (Snyder et al., 2014). Our present study bolsters the finding that a subset of patients with microsatellite-stable pancreatic cancer harbor predicted MHC class I-restricted neoepitopes, even in advanced/metastatic disease. Additionally, by expanding the search space for potential neoepitopes to include in-frame insertion/deletion and frameshift mutations, we demonstrate that the landscape of potentially immunogenic neoepitopes in PDAC can be substantially increased. Although our neoepitope predictions do not directly assess immunogenicity, our findings are in line with numerous prior reports that have identified endogenous neoantigen-reactive CD8⁺ TILs from a subset of human PDAC patients (Gros et al., 2019; Meng et al., 2019; Parkhurst et al., 2019; Sakellariou-Thompson et al., 2017); however, the absolute proportion of human patients with immunogenic neoantigens remains to be determined.

To model this subset of patients, we generated multiple orthogonal preclinical models of neoantigen-expressing pancreatic cancer and demonstrated that PDAC undergoes all three phases of immunosurveillance (Dunn et al., 2004), with a subset of animals successfully evading immune clearance despite continued tumor-specific expression of a high-affinity neoantigen. While previous efforts have explored neoantigen expression in preclinical PDAC models (Evans et al., 2016; Hegde et al., 2020), both orthotopic transplantation of pancreatic organoids and retrograde pancreatic duct delivery of lentiviruses offer the flexibility and genetic tractability to interrogate new and diverse neoantigen(s) and leverage CRISPR-mediated gene perturbations to rapidly evaluate biological hypotheses. The incorporation of defined neoantigens facilitates the tracking and immunophenotyping of tumor-reactive CD8⁺ T cells, but these are not the only potential (neo)antigens present in these tumors. mScarlet, used as a surrogate for neoantigen expression, is a foreign protein and may also contribute MHC class I-restricted and/or class II-restricted neoantigens. Furthermore, there may be additional mutations accumulated during tumorigenesis. Future studies will be needed to evaluate the functional consequences of varying affinity neoantigens and defined MHC class II neoantigens in PDAC. Additionally, it is important to note that KP;SIIN organoids do not express the neoantigen as part of a mature protein, and hence may not recapitulate all aspects of endogenous antigen processing.

Using scRNA-seq and flow cytometric profiling of immune-evasive murine PDAC, we uncovered multiple classes of CD8⁺ TILs with markers of dysfunction and identified similar populations of intratumoral CD8⁺ T cells in human PDAC, suggesting that these preclinical models accurately recapitulate a subset of human PDAC. While both murine and human PDAC prominently feature CD8⁺ TILs with markers of dysfunction, we also observed non-terminally exhausted CD8⁺ TILs and evidence of an ongoing intratumoral immune response. However, it is impor-

tant to point out that in the case of human PDAC we were unable to assess the tumor reactivity of these populations. We likewise demonstrated the presence of “progenitor-like” (PD1⁺TCF1^{hi}) CD8⁺ TILs in human and murine PDAC, the latter of which are found within the neoantigen-specific TIL compartment, suggesting the potential for re-invigoration with ICB. The near complete lack of clinical benefit provided by PD-(L)1-directed ICB in human PDAC, an observation that is accurately recapitulated in our preclinical models, suggests that PDAC may employ additional mechanisms of immune evasion that serve to limit the anti-tumor immune response.

Our characterization of the neoantigen-specific immune response has functionally implicated the co-inhibitory receptor TIGIT, and its high-affinity ligand CD155, as a critical axis driving PDAC immune evasion. We demonstrate that CD155 is expressed on the surface of murine and human PDAC tumor cells, both *in vivo* and *ex vivo*. As CD155 has been reported to be upregulated by oncogenic KRAS in cell culture (Ikeda et al., 2003; Nishi et al., 2020), it is tempting to speculate that the CD155/TIGIT axis might represent a critical immune checkpoint in additional KRAS-driven tumors. Our data support this and also suggest a potential synergy between KRAS and TP53 mutations to upregulate CD155, further refining the complex regulation of this inhibitory ligand.

We also demonstrated that TIGIT is expressed on a subset of human and murine TILs, and in the latter case further delineated that tumor-reactive (neoantigen-specific) CD8⁺ TILs express high levels of TIGIT. Tumor-specific overexpression of CD155 in neoantigen-expressing autochthonous pancreatic cancer leads to an increased proportion of immune-evasive tumors, and these results can be recapitulated using an agonistic TIGIT antibody. Thus, increased signaling through the CD155/TIGIT axis is sufficient to promote immune evasion in PDAC. While we were able to functionally interrogate the CD155/TIGIT axis in murine PDAC, it is important to emphasize that all of our human analyses are correlative. Clinical evaluation of TIGIT blockade in human pancreatic cancer patients will be needed to elucidate the functional significance of this immune axis in human PDAC immune evasion. In addition to CD8⁺ T cells, TIGIT is also expressed on regulatory T cells and natural killer cells (Anderson et al., 2016; Kurtulus et al., 2015), and TIGIT-mediated ligation of CD155 on the surface of dendritic cells can promote a more tolerogenic cytokine milieu and impact T cell priming (Yu et al., 2009). Future studies will be needed to dissect the contributions of the CD155/TIGIT axis within these various cell compartments and their roles in PDAC immune evasion.

A number of scenarios have been proposed to explain how PDAC evades the anti-tumor immune response, and previous reports have implicated almost every step in the cancer-immunity cycle (Chen and Mellman, 2013). PDAC may bypass immune surveillance through loss of MHC class I surface expression (Yamamoto et al., 2020), exclusion of T cells (Joyce and Fearon, 2015; Li et al., 2018; Stromnes et al., 2017), induction of dysfunctional T cell programs (Steele et al., 2020; Stromnes et al., 2017), deficiencies in type I conventional dendritic cells (Hegde et al., 2020; Lin et al., 2020), and/or recruitment of immune-suppressive cell populations (Bayne et al., 2012; Beatty et al., 2015; Stromnes et al., 2014). However, the majority of prior studies have been unable to isolate the effects of tumor and/or

microenvironmental perturbations on the neoantigen-specific immune response. While our data support a crucial role for neoantigen-specific T cell dysfunction and the CD155/TIGIT axis in PDAC immune evasion, it is likely that multiple facets of the tumor-immunity cycle are disrupted in PDAC. Indeed, we observed areas of T cell exclusion within immune-evasive animals in our model systems, suggesting that this may also contribute to immune escape in a subset of animals. Additionally, beyond the CD155/TIGIT axis, we uncovered multiple states of dysfunction within the neoantigen-specific TIL compartment, which can be functionally interrogated in future studies.

Immune modulation has emerged as a promising therapeutic strategy for numerous tumor types, but rationally guided combinatorial strategies that boost the endogenous anti-tumor immune response and prevent T cell exhaustion are likely necessary in PDAC (Johnson et al., 2017). CD40 agonism has been extensively evaluated in preclinical PDAC models (Byrne and Vonderheide, 2016; Ma et al., 2019; Morrison et al., 2020; Winoograd et al., 2015) and combination therapy using PD-1/CD40a + cytotoxic chemotherapy has demonstrated early-stage clinical promise in PDAC patients (Vonderheide, 2020; O'Hara et al., 2021). Using multi-arm, randomized, and blinded preclinical trials, we demonstrate that TIGIT/PD-1 co-blockade plus CD40 agonism can reinvigorate an effective anti-tumor immune response in a subset of animals with immune-evasive PDAC. Mechanistically, we observed increased expression of inhibitory ligands following CD40 agonist containing combination immunotherapy. While tumor cells displayed elevated CD155 expression at baseline, we observed increased PD-L1 and CD155 expression within the TAS/TSI following treatment. These results suggest that the PD-1/PD-L1 and CD155/TIGIT axes may represent non-redundant mechanisms of acquired resistance to CD40 agonist-based therapies and further support strategies that leverage co-blockade of these inhibitory axes. In addition, our efforts point to a potential role for MDSC-mediated T cell exclusion as a mechanism of resistance to TIGIT/PD-1/CD40a. Future studies in additional preclinical PDAC models will evaluate the requirement for high-affinity neoantigens in mediating this response and directly address additional combination strategies to overcome these resistance mechanisms. While our profiling of the neoantigen-specific immune response in PDAC nominates additional immune checkpoints for future preclinical evaluation, combinatorial targeting of TIGIT/PD-1/CD40a represents a particularly promising approach for rapid clinical translation.

STAR★METHODS

Detailed methods are provided in the online version of this paper and include the following:

- **KEY RESOURCES TABLE**
- **RESOURCE AVAILABILITY**
 - Lead contact
 - add Materials availability
 - Data and code availability
- **EXPERIMENTAL MODEL AND SUBJECT DETAILS**
 - Mice
 - mESC generation and CRISPR-assisted targeting
 - Organoid generation and characterization

- T cell culture
- Organoid + CD8 T cell co-culture
- Orthotopic transplantation
- Small rodent ultrasound
- Preclinical trials
- Retrograde pancreatic duct delivery
- **METHOD DETAILS**
 - Molecular cloning
 - Lentiviral production/titering
 - Flow cytometry
 - Flow cytometry of human PDAC
 - Immunohistochemistry and pathology review
 - Nanostring GeoMx digital spatial profiling
 - Single-cell RNA sequencing
 - Single-cell RNA sequencing analysis
 - Gene module analysis
- **QUANTIFICATION AND STATISTICAL ANALYSIS**
 - Statistical analyses
 - Clinical data analysis
 - Neoepitope prediction
 - scRNA-seq analysis of human PDAC

SUPPLEMENTAL INFORMATION

Supplemental information can be found online at <https://doi.org/10.1016/j.ccell.2021.07.007>.

ACKNOWLEDGMENTS

We thank the entire Jacks laboratory with specific thanks to M. Burger and D. Canner for helpful discussions and technical assistance, and K. Yee, J. Teixeira, K. Anderson, and M. Magendantz for administrative support. We thank A. Aguirre and B. Wolpin for providing raw data and mutation calls for DFCI-PancSeq. We thank E. Miller for helpful discussions on NanoString GeoMx. This work was supported by the Howard Hughes Medical Institute, NCI Cancer Center support grant P30-CA14051, the Lustgarten Foundation Pancreatic Cancer Research Laboratory at MIT, DFHCC SPORE in Gastrointestinal Cancer Career Enhancement Award (W.A.F.-P.), the Stand Up To Cancer-Lustgarten Foundation Pancreatic Cancer Interception Translational Cancer Research Grant (SU2C-AACR-DT25-17, W.A.F.-P., T.J.), the Stand Up To Cancer Golden Arrow Early Career Scientist Award (GA-6182, W.A.F.-P.), Damon Runyon (P.M.K.W., A.M.J.), and NIH pre-doctoral training grant (T32GM007287, Z.A.E., L.J.L.). Stand Up To Cancer is a program of the Entertainment Industry Foundation. Research grants are administered by the American Association for Cancer Research, the scientific partner of SU2C. We thank the Koch Institute's Robert A. Swanson (1969) Biotechnology Center for technical support, specifically flow cytometry, histology, and preclinical imaging core facilities.

AUTHOR CONTRIBUTIONS

W.A.F.-P. and T.J. conceived, designed, and directed the study; W.A.F.-P., L.J.L., N.B.P., A.P.G., and K.L.M. performed all types of experiments reported in the study; Z.A.E. designed and constructed the neoepitope prediction pipeline and conducted all scRNA-seq bioinformatic analyses and neoepitope predictions; A.B. conducted bioinformatic analyses and provided conceptual advice; G.E. provided organoid expertise; G.E., V.D., and O.H.Y. provided human biospecimens; W.A.F.-P., L.L., and N.B.P. performed murine surgeries; G.E. and R.T.B. provided pathology expertise; W.A.F.-P., A.P.G., and W.M.R. conducted murine embryonic stem cell targeting; W.L.H., T.D., and D.P. conducted scRNA-seq; T.D.H., P.D., and J.W.R. provided NanoString GeoMx biostatistical support; J.M.S., A.M.J., P.M.K.W., O.H.Y., A.R., and A.B. provided conceptual advice; W.A.F.-P., L.J.L., Z.A.E., and T.J. wrote the manuscript with comments from all authors.

DECLARATION OF INTERESTS

T.J. is a member of the Board of Directors of Amgen and Thermo Fisher Scientific, and a co-Founder of Dragonfly Therapeutics and T2 Biosystems. T.J. serves on the Scientific Advisory Board of Dragonfly Therapeutics, SQZ Biotech, and Skyhawk Therapeutics. T.J. is also President of Break Through Cancer. His laboratory currently receives funding from Johnson & Johnson and The Lustgarten Foundation; funds from the Lustgarten Foundation supported the research described in this manuscript. A.R. is a founder and equity holder of Celsius Therapeutics, an equity holder in Immunitas Therapeutics and until August 31, 2020, was an SAB member of Syros Pharmaceuticals, Neogene Therapeutics, Asimov and Thermo Fisher Scientific. From August 1, 2020, A.R. is an employee of Genentech, a member of the Roche Group. A.R. and Regev lab members' work was conducted at the Broad Institute, unrelated to these later affiliations. T.D.H., P.D., and J.W.R. are employees and stockholders at NanoString Technologies, Inc. None of these affiliations represent a conflict of interest with respect to the design or execution of this study or interpretation of data presented in this manuscript.

Received: December 11, 2020

Revised: April 26, 2021

Accepted: July 12, 2021

Published: August 5, 2021

REFERENCES

- Aguirre, A.J., Nowak, J.A., Camarda, N.D., Moffitt, R.A., Ghazani, A.A., Hazar-Rethinam, M., Raghavan, S., Kim, J., Brais, L.K., Ragon, D., et al. (2018). Real-time genomic characterization of advanced pancreatic cancer to enable precision medicine. *Cancer Discov.* **8**, 1096–1111.
- Akama-Garren, E.H., Joshi, N.S., Tammela, T., Chang, G.P., Wagner, B.L., Lee, D.Y., Rideout, W.M., Papagiannakopoulos, T., Xue, W., and Jacks, T. (2016). A modular assembly platform for rapid generation of DNA constructs. *Sci. Rep.* **6**, 16836.
- Alspach, E., Lussier, D.M., Miceli, A.P., Kizhvato, I., DuPage, M., Luoma, A.M., Meng, W., Lichti, C.F., Esaulova, E., Vomund, A.N., et al. (2019). MHC-II neoantigens shape tumour immunity and response to immunotherapy. *Nature* **574**, 696–701.
- Anderson, A.C., Joller, N., and Kuchroo, V.K. (2016). Lag-3, Tim-3, and TIGIT: Co-inhibitory receptors with specialized functions in immune regulation. *Immunity* **44**, 989–1004.
- Andreatta, M., and Nielsen, M. (2016). Gapped sequence alignment using artificial neural networks: application to the MHC class I system. *Bioinformatics* **32**, 511–517.
- Bailey, P., Chang, D.K., Forget, M.A., Lucas, F.A.S., Alvarez, H.A., Haymaker, C., Chattopadhyay, C., Kim, S.H., Ekmekcioglu, S., Grimm, E.A., et al. (2016). Exploiting the neoantigen landscape for immunotherapy of pancreatic ductal adenocarcinoma. *Sci. Rep.* **6**, 35848.
- Balachandran, V.P., Łuksza, M., Zhao, J.N., Makarov, V., Moral, J.A., Remark, R., Herbst, B., Askan, G., Bhanot, U., Senbabaoglu, Y., et al. (2017). Identification of unique neoantigen qualities in long-term survivors of pancreatic cancer. *Nature* **551**, 512–516.
- Bankhead, P., Loughrey, M.B., Fernández, J.A., Dombrowski, Y., McArt, D.G., Dunne, P.D., McQuaid, S., Gray, R.T., Murray, L.J., Coleman, H.G., et al. (2017). QuPath: open source software for digital pathology image analysis. *Sci. Rep.* **7**, 16878.
- Bauer, D.C., Zadoorian, A., Wilson, L.O.W., and Thorne, N.P. (2018). Evaluation of computational programs to predict HLA genotypes from genomic sequencing data. *Brief. Bioinform.* **19**, 179–187.
- Bayne, L.J., Beatty, G.L., Jhala, N., Clark, C.E., Rhim, A.D., Stanger, B.Z., and Vonderheide, R.H. (2012). Tumor-derived granulocyte-macrophage colony-stimulating factor regulates myeloid inflammation and T cell immunity in pancreatic cancer. *Cancer Cell* **21**, 822–835.
- Beatty, G.L., Winograd, R., Evans, R.A., Long, K.B., Luque, S.L., Lee, J.W., Clendenin, C., Gladney, W.L., Knoblock, D.M., Guirnalda, P.D., et al. (2015). Exclusion of T Cells from pancreatic carcinomas in mice is regulated by Ly6C(low) F4/80(+) extratumoral macrophages. *Gastroenterology* **149**, 201–210.
- Becht, E., McInnes, L., Healy, J., Dutertre, C.A., Kwok, I.W.H., Ng, L.G., Ginhoux, F., and Newell, E.W. (2019). Dimensionality reduction for visualizing single-cell data using UMAP. *Nat. Biotechnol.* **37**, 38–47.
- Benjamini, Y., and Hochberg, Y. (1995). Controlling the false discovery rate: a practical and powerful approach to multiple testing. *J. R. Stat. Soc. Ser. B* **57**, 289–300.
- Bindels, D.S., Haarbosch, L., Van Weeren, L., Postma, M., Wiese, K.E., Mastop, M., Aumonier, S., Gotthard, G., Royant, A., Hink, M.A., et al. (2016). MScarlet: a bright monomeric red fluorescent protein for cellular imaging. *Nat. Methods* **14**, 53–56.
- Blank, C.U., Haining, W.N., Held, W., Hogan, P.G., Kallies, A., Lugli, E., Lynn, R.C., Philip, M., Rao, A., Restifo, N.P., et al. (2019). Defining 'T cell exhaustion'. *Nat. Rev. Immunol.* **19**, 665–674.
- Boegel, S., Löwer, M., Schäfer, M., Bukur, T., de Graaf, J., Boisguérin, V., Türeci, Ö., Diken, M., Castle, J.C., and Sahin, U. (2012). HLA typing from RNA-Seq sequence reads. *Genome Med.* **4**, 102.
- Boj, S.F., Hwang, C.-I., Baker, L.A., Chio, I.I.C., Engle, D.D., Corbo, V., Jager, M., Ponz-Sarvisé, M., Tiriac, H., Spector, M.S., et al. (2015). Organoid models of human and mouse ductal pancreatic cancer. *Cell* **160**, 324–338.
- Brahmer, J.R., Tykodi, S.S., Chow, L.Q.M., Hwu, W.-J., Topalian, S.L., Hwu, P., Drake, C.G., Camacho, L.H., Kauh, J., Odunsi, K., et al. (2012). Safety and activity of anti-PD-L1 antibody in patients with advanced cancer. *N. Engl. J. Med.* **366**, 2455–2465.
- Butler, A., Hoffman, P., Smibert, P., Papalexi, E., and Satija, R. (2018). Integrating single-cell transcriptomic data across different conditions, technologies, and species. *Nat. Biotechnol.* **36**, 411–420.
- Byrne, K.T., and Vonderheide, R.H. (2016). CD40 stimulation obviates innate sensors and drives T cell immunity in cancer. *Cell Rep.* **15**, 2719–2732.
- Cancer Genome Atlas Research Network (2017). Integrated genomic characterization of pancreatic ductal adenocarcinoma. *Cancer Cell* **32**, 185–203.e13.
- Chavez, A., Scheiman, J., Vora, S., Pruitt, B.W., Tuttle, M., P R Iyer, E., Lin, S., Kiani, S., Guzman, C.D., Wiegand, D.J., et al. (2015). Highly efficient Cas9-mediated transcriptional programming. *Nat. Methods* **12**, 326–328.
- Chen, D.S., and Mellman, I. (2013). Oncology meets immunology: the cancer-immunity cycle. *Immunity* **39**, 1–10.
- Chen, X., Schulz-Trieglaff, O., Shaw, R., Barnes, B., Schlesinger, F., Källberg, M., Cox, A.J., Kruglyak, S., and Saunders, C.T. (2016). Manta: rapid detection of structural variants and indels for germline and cancer sequencing applications. *Bioinformatics* **32**, 1220–1222.
- Chihara, N., Madi, A., Kondo, T., Zhang, H., Acharya, N., Singer, M., Nyman, J., Marjanovic, N.D., Kowalczyk, M.S., Wang, C., et al. (2018). Induction and transcriptional regulation of the co-inhibitory gene module in T cells. *Nature* **558**, 454–459.
- Chiou, S.-H., Winters, I.P., Wang, J., Naranjo, S., Dudgeon, C., Tamburini, F.B., Brady, J.J., Yang, D., Grüner, B.M., Chuang, C.-H., et al. (2015). Pancreatic cancer modeling using retrograde viral vector delivery and in vivo CRISPR/Cas9-mediated somatic genome editing. *Genes Dev.* **29**, 1576–1585.
- Church, G.M., and Gilbert, W. (1984). Genomic sequencing. *Proc. Natl. Acad. Sci. U S A* **81**, 1991–1995.
- Collisson, E.A., Campbell, J.D., Brooks, A.N., Berger, A.H., Lee, W., Chmielecki, J., Beer, D.G., Cope, L., Creighton, C.J., Danilova, L., et al. (2014). Comprehensive molecular profiling of lung adenocarcinoma: the cancer genome atlas research network. *Nature* **511**, 543–550.
- Conroy, T., Desseigne, F., Ychou, M., Bouché, O., Guimbaud, R., Bécouarn, Y., Adenis, A., Raouf, J.-L., Gourgou-Bourgade, S., de la Fouchardière, C., et al. (2011). FOLFIRINOX versus gemcitabine for metastatic pancreatic cancer. *N. Engl. J. Med.* **364**, 1817–1825.
- Danecek, P., Auton, A., Abecasis, G., Albers, C.A., Banks, E., DePristo, M.A., Handsaker, R.E., Lunter, G., Marth, G.T., Sherry, S.T., et al. (2011). The variant call format and VCFtools. *Bioinformatics* **27**, 2156–2158.
- Dixon, K.O., Schorer, M., Nevin, J., Etmnan, Y., Amoozgar, Z., Kondo, T., Kurtulus, S., Kassam, N., Sobel, R.A., Fukumura, D., et al. (2018). Functional

anti-TIGIT antibodies regulate development of autoimmunity and antitumor immunity. *J. Immunol.* **200**, 3000–3007.

Doering, T.A., Crawford, A., Angelosanto, J.M., Paley, M.A., Ziegler, C.G., and Wherry, E.J. (2012). Network analysis reveals centrally connected genes and pathways involved in CD8⁺ T cell exhaustion versus memory. *Immunity* **37**, 1130–1144.

Dunn, G.P., Old, L.J., and Schreiber, R.D. (2004). The three Es of cancer immunoeediting. *Annu. Rev. Immunol.* **22**, 329–360.

Durinck, S., Moreau, Y., Kasprzyk, A., Davis, S., De Moor, B., Brazma, A., and Huber, W. (2005). BioMart and Bioconductor: a powerful link between biological databases and microarray data analysis. *Bioinformatics* **21**, 3439–3440.

Durinck, S., Spellman, P.T., Birney, E., and Huber, W. (2009). Mapping identifiers for the integration of genomic datasets with the R/Bioconductor package biomaRt. *Nat. Protoc.* **4**, 1184–1191.

Eso, Y., Shimizu, T., Takeda, H., Takai, A., and Marusawa, H. (2020). Microsatellite instability and immune checkpoint inhibitors: toward precision medicine against gastrointestinal and hepatobiliary cancers. *J. Gastroenterol.* **55**, 15–26.

Evans, R.A., Diamond, M.S., Rech, A.J., Chao, T., Richardson, M.W., Lin, J.H., Bajor, D.L., Byrne, K.T., Stanger, B.Z., Riley, J.L., et al. (2016). Lack of immunoeediting in murine pancreatic cancer reversed with neoantigen. *JCI Insight* **1**, e88328.

Fan, J., Salathia, N., Liu, R., Kaeser, G.E., Yung, Y.C., Herman, J.L., Kaper, F., Fan, J.B., Zhang, K., Chun, J., et al. (2016). Characterizing transcriptional heterogeneity through pathway and gene set overdispersion analysis. *Nat. Methods* **13**, 241–244.

Gao, H., Korn, J.M., Ferretti, S., Monahan, J.E., Wang, Y., Singh, M., Zhang, C., Schnell, C., Yang, G., Zhang, Y., et al. (2015). High-throughput screening using patient-derived tumor xenografts to predict clinical trial drug response. *Nat. Med.* **21**, 1318–1325.

Gao, J., Aksoy, B.A., Dogrusoz, U., Dresdner, G., Gross, B., Sumer, S.O., Sun, Y., Jacobsen, A., Sinha, R., Larsson, E., et al. (2013). Integrative analysis of complex cancer genomics and clinical profiles using the cBioPortal. *Sci. Signal.* **6**, pii1.

Gibson, D.G., Young, L., Chuang, R.Y., Venter, J.C., Hutchison, C.A., and Smith, H.O. (2009). Enzymatic assembly of DNA molecules up to several hundred kilobases. *Nat. Methods* **6**, 343–345.

Gros, A., Tran, E., Parkhurst, M.R., Ilyas, S., Pasetto, A., Groh, E.M., Robbins, P.F., Yossef, R., Garcia-Garjito, A., Fajardo, C.A., et al. (2019). Recognition of human gastrointestinal cancer neoantigens by circulating PD-1⁺ lymphocytes. *J. Clin. Invest.* **129**, 4992–5004.

Gubin, M.M., Zhang, X., Schuster, H., Caron, E., Ward, J.P., Noguchi, T., Ivanova, Y., Hundal, J., Arthur, C.D., Krebber, W.J., et al. (2014). Checkpoint blockade cancer immunotherapy targets tumour-specific mutant antigens. *Nature* **515**, 577–581.

Haeussler, M., Zweig, A.S., Tyner, C., Speir, M.L., Rosenbloom, K.R., Raney, B.J., Lee, C.M., Lee, B.T., Hinrichs, A.S., Gonzalez, J.N., et al. (2019). The UCSC Genome Browser database: 2019 update. *Nucleic Acids Res.* **47**, D853–D858.

Hafemeister, C., and Satija, R. (2019). Normalization and variance stabilization of single-cell RNA-seq data using regularized negative binomial regression. *Genome Biol.* **20**, 296.

Hao, Z., and Rajewsky, K. (2001). Homeostasis of peripheral B cells in the absence of B cell influx from the bone marrow. *J. Exp. Med.* **194**, 1151–1163.

Harjunpää, H., and Guillerey, C. (2020). TIGIT as an emerging immune checkpoint. *Clin. Exp. Immunol.* **200**, 108–119.

Hegde, S., Krisnawan, V.E., Herzog, B.H., Zuo, C., Breden, M.A., Knolhoff, B.L., Hogg, G.D., Tang, J.P., Baer, J.M., Mpoy, C., et al. (2020). Dendritic cell paucity leads to dysfunctional immune surveillance in pancreatic cancer. *Cancer Cell* **37**, 289–307.e9.

Hippenmeyer, S., Youn, Y.H., Moon, H.M., Miyamichi, K., Zong, H., Wynshaw-Boris, A., and Luo, L. (2010). Genetic mosaic dissection of Lis1 and Ndel1 in neuronal migration. *Neuron* **68**, 695–709.

Hirsch, F.R., Varella-Garcia, M., Bunn, P.A., Di Maria, M.V., Veve, R., Bremnes, R.M., Barón, A.E., Zeng, C., and Franklin, W.A. (2003). Epidermal growth factor receptor in non-small-cell lung carcinomas: correlation between gene copy number and protein expression and impact on prognosis. *J. Clin. Oncol.* **21**, 3798–3807.

Hoadley, K.A., Yau, C., Hinoue, T., Wolf, D.M., Lazar, A.J., Drill, E., Shen, R., Taylor, A.M., Cherniack, A.D., Thorsson, V., et al. (2018). Cell-of-Origin patterns dominate the molecular classification of 10,000 tumors from 33 types of cancer. *Cell* **173**, 291–304.e6.

Von Hoff, D.D., Ervin, T., Arena, F.P., Chiorean, E.G., Infante, J., Moore, M., Seay, T., Tjuland, S.A., Ma, W.W., Saleh, M.N., et al. (2013). Increased survival in pancreatic cancer with nab-paclitaxel plus gemcitabine. *N. Engl. J. Med.* **369**, 1691–1703.

Hogquist, K.A., Jameson, S.C., Heath, W.R., Howard, J.L., Bevan, M.J., and Carbone, F.R. (1994). T cell receptor antagonist peptides induce positive selection. *Cell* **76**, 17–27.

Horlbeck, M.A., Gilbert, L.A., Villalta, J.E., Adamson, B., Pak, R.A., Chen, Y., Fields, A.P., Park, C.Y., Corn, J.E., Kampmann, M., et al. (2016). Compact and highly active next-generation libraries for CRISPR-mediated gene repression and activation. *eLife* **5**, e19760.

Hundal, J., Kiwala, S., McMichael, J., Miller, C.A., Xia, H., Wollam, A.T., Liu, C.J., Zhao, S., Feng, Y.Y., Graubert, A.P., et al. (2020). PVACTools: a computational toolkit to identify and visualize cancer neoantigens. *Cancer Immunol. Res.* **8**, 409–420.

Hung, A.L., Maxwell, R., Theodoros, D., Belcaid, Z., Mathios, D., Luksik, A.S., Kim, E., Wu, A., Xia, Y., Garzon-Muvdi, T., et al. (2018). TIGIT and PD-1 dual checkpoint blockade enhances antitumor immunity and survival in GBM. *Oncoimmunology* **7**, e1466769.

Ihaka, R., and Gentleman, R. (1996). R: a language for data analysis and graphics. *J. Comput. Graph. Stat.* **5**, 299–314.

Ikeda, W., Kakunaga, S., Itoh, S., Shingai, T., Takekuni, K., Satoh, K., Inoue, Y., Hamaguchi, A., Morimoto, K., Takeuchi, M., et al. (2003). TAGE4/nectin-like molecule-5 heterophilically trans-interacts with cell adhesion molecule nectin-3 and enhances cell migration. *J. Biol. Chem.* **278**, 28167–28172.

Jackson, E.L., Willis, N., Mercer, K., Bronson, R.T., Crowley, D., Montoya, R., Jacks, T., and Tuveson, D.A. (2001). Analysis of lung tumor initiation and progression using conditional expression of oncogenic K-ras. *Genes Dev.* **15**, 3243–3248.

Johnson, B.A., Yarchoan, M., Lee, V., Laheru, D.A., and Jaffee, E.M. (2017). Strategies for increasing pancreatic tumor immunogenicity. *Clin. Cancer Res.* **23**, 1656–1669.

Joyce, J.A., and Fearon, D.T. (2015). T cell exclusion, immune privilege, and the tumor microenvironment. *Science* **348**, 74–80.

Jurtz, V., Paul, S., Andreatta, M., Marcatili, P., Peters, B., and Nielsen, M. (2017). NetMHCpan-4.0: improved peptide-MHC class I interaction predictions integrating eluted ligand and peptide binding affinity data. *J. Immunol.* **199**, 3360–3368.

Kim, H.J., Wang, X., Radfar, S., Sproule, T.J., Roopenian, D.C., and Cantor, H. (2011). CD8⁺ T regulatory cells express the Ly49 class I MHC receptor and are defective in autoimmune prone B6-Yaa mice. *Proc. Natl. Acad. Sci. U S A* **108**, 2010–2015.

Kim, M.P., Evans, D.B., Wang, H., Abbruzzese, J.L., Fleming, J.B., and Gallick, G.E. (2009). Generation of orthotopic and heterotopic human pancreatic cancer xenografts in immunodeficient mice. *Nat. Protoc.* **4**, 1670–1680.

Kim, S., Scheffler, K., Halpern, A.L., Bekritsky, M.A., Noh, E., Källberg, M., Chen, X., Kim, Y., Beyter, D., Krusche, P., et al. (2018). Strelka2: fast and accurate calling of germline and somatic variants. *Nat. Methods* **15**, 591–594.

Kolde, R. (2019). Pheatmap: Pretty Heatmaps. <https://rdrr.io/cran/pheatmap/>.

Kurtulus, S., Sakuishi, K., Ngiow, S.F., Joller, N., Tan, D.J., Teng, M.W.L., Smyth, M.J., Kuchroo, V.K., and Anderson, A.C. (2015). TIGIT predominantly regulates the immune response via regulatory T cells. *J. Clin. Invest.* **125**, 4053–4062.

- Kuznetsova, A., Brockhoff, P.B., and Christensen, R.H.B. (2017). ImerTest package: tests in linear mixed effects models. *J. Stat. Software Artic.* **82**. <https://doi.org/10.18637/jss.v082.i13>.
- Lawrence, M.S., Stojanov, P., Polak, P., Kryukov, G.V., Cibulskis, K., Sivachenko, A., Carter, S.L., Stewart, C., Mermel, C.H., Roberts, S.A., et al. (2013). Mutational heterogeneity in cancer and the search for new cancer-associated genes. *Nature* **499**, 214–218.
- Li, H., Handsaker, B., Wysoker, A., Fennell, T., Ruan, J., Homer, N., Marth, G., Abecasis, G., and Durbin, R. (2009). The sequence alignment/map format and SAMtools. *Bioinformatics* **25**, 2078–2079.
- Li, J., Byrne, K.T., Yan, F., Yamazoe, T., Chen, Z., Baslan, T., Richman, L.P., Lin, J.H., Sun, Y.H., Rech, A.J., et al. (2018). Tumor cell-intrinsic factors underlie heterogeneity of immune cell infiltration and response to immunotherapy. *Immunity* **49**, 178–193.e7.
- Liang, S.C., Latchman, Y.E., Buhlmann, J.E., Tomczak, M.F., Horwitz, B.H., Freeman, G.J., and Sharpe, A.H. (2003). Regulation of PD-1, PD-L1, and PD-L2 expression during normal and autoimmune responses. *Eur. J. Immunol.* **33**, 2706–2716.
- Lin, J.H., Huffman, A.P., Wattenberg, M.M., Walter, D.M., Carpenter, E.L., Feldser, D.M., Beatty, G.L., Furth, E.E., and Vonderheide, R.H. (2020). Type 1 conventional dendritic cells are systemically dysregulated early in pancreatic carcinogenesis. *J. Exp. Med.* **217**, e20190673.
- Liudahl, S.M., Betts, C.B., Sivagnanam, S., Morales-Oyarvide, V., da Silva, A., Yuan, C., Hwang, S., Grossblatt-Wait, A., Leis, K.R., Larson, W., et al. (2021). Leukocyte heterogeneity in pancreatic ductal adenocarcinoma: phenotypic and spatial features associated with clinical outcome. *Cancer Discov.* <https://doi.org/10.1158/2159-8290.CD-20-0841>.
- Ma, H.S., Poudel, B., Torres, E.R., Sidhom, J.W., Robinson, T.M., Christmas, B., Scott, B., Cruz, K., Woolman, S., Wall, V.Z., et al. (2019). A CD40 agonist antibody reprogram the microenvironment of nonimmunogenic tumors to allow T-cell-mediated anticancer activity. *Cancer Immunol. Res.* **7**, 428–442.
- Marino, S., Vooijs, M., Van Der Gulden, H., Jonkers, J., and Berns, A. (2000). Induction of medulloblastomas in p53-null mutant mice by somatic inactivation of Rb in the external granular layer cells of the cerebellum. *Genes Dev.* **14**, 994–1004.
- McInnes, L., Healy, J., Saul, N., and Großberger, L. (2018). UMAP: Uniform Manifold Approximation and Projection. *J. Open Source Softw.* **3**. <https://doi.org/10.21105/joss.00861>.
- McLaren, W., Gil, L., Hunt, S.E., Riat, H.S., Ritchie, G.R.S., Thormann, A., Flicek, P., and Cunningham, F. (2016). The Ensembl variant effect predictor. *Genome Biol.* **17**, 122.
- Meng, Q., Valentini, D., Rao, M., Moro, C.F., Paraschoudi, G., Jäger, E., Dodo, E., Rangelova, E., del Chiaro, M., and Maeurer, M. (2019). Neopeptide targets of tumour-infiltrating lymphocytes from patients with pancreatic cancer. *Br. J. Cancer* **120**, 97–108.
- De Meo, P., Ferrara, E., Fiumara, G., and Provetti, A. (2011). Generalized Louvain method for community detection in large networks. In *International Conference on Intelligent Systems Design and Applications (ISDA)*, pp. 88–93.
- Miller, B.C., Sen, D.R., Al Abosy, R., Bi, K., Virkud, Y.V., LaFleur, M.W., Yates, K.B., Lako, A., Felt, K., Naik, G.S., et al. (2019). Subsets of exhausted CD8⁺ T cells differentially mediate tumor control and respond to checkpoint blockade. *Nat. Immunol.* **20**, 326–336.
- Morrison, A.H., Diamond, M.S., Hay, C.A., Byrne, K.T., and Vonderheide, R.H. (2020). Sufficiency of CD40 activation and immune checkpoint blockade for T cell priming and tumor immunity. *Proc. Natl. Acad. Sci. U S A* **117**, 8022–8031.
- Muzny, D.M., Bainbridge, M.N., Chang, K., Dinh, H.H., Drummond, J.A., Fowler, G., Kovar, C.L., Lewis, L.R., Morgan, M.B., Newsham, I.F., et al. (2012). Comprehensive molecular characterization of human colon and rectal cancer. *Nature* **487**, 330–337.
- Narzisi, G., O’Rawe, J.A., Iossifov, I., Fang, H., Lee, Y.H., Wang, Z., Wu, Y., Lyon, G.J., Wigler, M., and Schatz, M.C. (2014). Accurate de novo and transmitted indel detection in exome-capture data using microassembly. *Nat. Methods* **11**, 1033–1036.
- Nishi, K., Ishikura, S., Umebayashi, M., Morisaki, T., Inozume, T., Kinugasa, T., Aoki, M., Nimura, S., Swain1, A., Yoshida, Y., et al. (2020). Mutant KRAS promotes NKG2D⁺ T cell infiltration and CD155 dependent immune evasion. *Anticancer Res.* **40**, 4663–4674.
- O’Hara, M.H., O’Reilly, E.M., Varadhachary, G., Wolff, R.A., Wainberg, Z.A., Ko, A.H., Fisher, G., Rahma, O., Lyman, J.P., Cabanski, C.R., et al. (2021). CD40 agonistic monoclonal antibody APX005M (sotigalimab) and chemotherapy, with or without nivolumab, for the treatment of metastatic pancreatic adenocarcinoma: an open-label, multicentre, phase 1b study. *Lancet Oncol.* **22**, 118–131.
- O’Reilly, E.M., Oh, D.Y., Dhani, N., Renouf, D.J., Lee, M.A., Sun, W., Fisher, G., Hezel, A., Chang, S.C., Vlahovic, G., et al. (2019). Durvalumab with or without Tremelimumab for patients with metastatic pancreatic ductal adenocarcinoma: a phase 2 randomized clinical trial. *JAMA Oncol.* **5**, 1431–1438.
- Parkhurst, M.R., Robbins, P.F., Tran, E., Prickett, T.D., Gartner, J.J., Li, J., Ivey, G., Li, Y.F., El-Gamil, M., Lalani, A., et al. (2019). Unique neoantigens arise from somatic mutations in patients with gastrointestinal cancers. *Cancer Discov.* **9**, 1022–1035.
- Peng, J., Sun, B.F., Chen, C.Y., Zhou, J.Y., Chen, Y.S., Chen, H., Liu, L., Huang, D., Jiang, J., Cui, G.S., et al. (2019). Single-cell RNA-seq highlights intra-tumoral heterogeneity and malignant progression in pancreatic ductal adenocarcinoma. *Cell Res.* **29**, 725–738.
- Peters, B., and Sette, A. (2005). Generating quantitative models describing the sequence specificity of biological processes with the stabilized matrix method. *BMC Bioinformatics* **6**, 132.
- Ribas, A., Butterfield, L.H., Amarni, S.N., Dissette, V.B., Kim, D., Meng, W.S., Miranda, G.A., Wang, H.J., McBride, W.H., Glaspy, J.A., et al. (2001). CD40 cross-linking bypasses the absolute requirement for CD4 T cells during immunization with melanoma antigen gene-modified dendritic cells. *Cancer Res.* **61**, 8787–8793.
- Rodriguez-Abreu, D., Lynne Johnson, M., Hussein, M.A., Cobo, M., Patel, A.J., Secen, N.M., Lee, K.H., Massuti, B., Hiret, S., Yang, J.C.-H., et al. (2020). Primary analysis of a randomized, double-blind, phase II study of the anti-TIGIT antibody tiragolumab (tira) plus atezolizumab (atezo) versus placebo plus atezo as first-line (1L) treatment in patients with PD-L1-selected NSCLC (CITYSCAPE). *J. Clin. Oncol.* **38** (suppl). abstract 9503. https://doi.org/10.1200/JCO.2020.38.15_suppl.9503.
- Rolink, A., Melchers, F., and Andersson, J. (1996). The SCID but not the RAG-2 gene product is required for $\Sigma\mu$ - $\Sigma\epsilon$ heavy chain class switching. *Immunity* **5**, 319–330.
- Ryan, D.P., Hong, T.S., and Bardeesy, N. (2014). Pancreatic adenocarcinoma. *N. Engl. J. Med.* **371**, 1039–1049.
- Sade-Feldman, M., Yizhak, K., Bjorgaard, S.L., Ray, J.P., de Boer, C.G., Jenkins, R.W., Lieb, D.J., Chen, J.H., Frederick, D.T., Barzily-Rokni, M., et al. (2018). Defining T cell states associated with response to checkpoint immunotherapy in melanoma. *Cell* **175**, 998–1013.e20.
- Sakellariou-Thompson, D., Forget, M.A., Creasy, C., Bernard, V., Zhao, L., Kim, Y.U., Hurd, M.W., Uraoka, N., Parra, E.R., Kang, Y., et al. (2017). 4-1BB agonist focuses CD8⁺ tumor-infiltrating T-cell growth into a distinct repertoire capable of tumor recognition in pancreatic cancer. *Clin. Cancer Res.* **23**, 7263–7275.
- Saligrama, N., Zhao, F., Sikora, M.J., Serratelli, W.S., Fernandes, R.A., Louis, D.M., Yao, W., Ji, X., Idoyaga, J., Mahajan, V.B., et al. (2019). Opposing T cell responses in experimental autoimmune encephalomyelitis. *Nature* **572**, 481–487.
- Sánchez-Rivera, F.J., Papagiannakopoulos, T., Romero, R., Tammela, T., Bauer, M.R., Bhatkar, A., Joshi, N.S., Subbaraj, L., Bronson, R.T., Xue, W., et al. (2014). Rapid modelling of cooperating genetic events in cancer through somatic genome editing. *Nature* **516**, 428–431.
- Sastra, S.A., and Olive, K.P. (2013). Quantification of murine pancreatic tumors by high-resolution ultrasound. *Methods Mol. Biol.* **980**, 249–266.

Schietinger, A., Philip, M., Krisnawan, V.E., Chiu, E.Y., Delrow, J.J., Basom, R.S., Lauer, P., Brockstedt, D.G., Knoblaugh, S.E., Hämmerling, G.J., et al. (2016). Tumor-specific T cell dysfunction is a dynamic antigen-driven differentiation program initiated early during tumorigenesis. *Immunity* *45*, 389–401.

Schnell, A., Bod, L., Madi, A., and Kuchroo, V.K. (2020). The yin and yang of co-inhibitory receptors: toward anti-tumor immunity without autoimmunity. *Cell Res.* *30*, 285–299.

Siddiqui, I., Schaeuble, K., Luther, S.A., Speiser, D.E., Correspondence, W.H., Chennupati, V., Fuentès Marraco, S.A., Calderon-Copete, S., Ferreira, D.P., Carmona, S.J., et al. (2019). Intratumoral Tcf1⁺ PD-1⁺ CD8⁺ T cells with stem-like properties promote tumor control in response to vaccination and checkpoint blockade immunotherapy. *Immunity* *50*, 195–211.e10.

Siegel, R.L., Miller, K.D., and Jemal, A. (2020). Cancer statistics, 2020. *CA Cancer J. Clin.* *70*, 7–30.

Singer, M., Wang, C., Cong, L., Marjanovic, N.D., Kowalczyk, M.S., Zhang, H., Nyman, J., Sakuishi, K., Kurtulus, S., Gennert, D., et al. (2016). A distinct gene module for dysfunction uncoupled from activation in tumor-infiltrating T cells. *Cell* *166*, 1500–1511.e9.

Snyder, A., Makarov, V., Merghoub, T., Yuan, J., Zaretsky, J.M., Desrichard, A., Walsh, L.A., Postow, M.A., Wong, P., Ho, T.S., et al. (2014). Genetic basis for clinical response to CTLA-4 blockade in melanoma. *N. Engl. J. Med.* *371*, 2189–2199.

Soriano, P. (1999). Generalized lacZ expression with the ROSA26 Cre reporter strain [1]. *Nat. Genet.* *21*, 70–71.

Steele, N.G., Carpenter, E.S., Kemp, S.B., Sirihorachai, V.R., The, S., Delrosario, L., Lazarus, J., Amir, E.D., Gunchick, V., Espinoza, C., et al. (2020). Multimodal mapping of the tumor and peripheral blood immune landscape in human pancreatic cancer. *Nat. Cancer* *1*, 1097–1112.

Stromnes, I.M., Brockenbrough, J.S., Izeradjene, K., Carlson, M.A., Cuevas, C., Simmons, R.M., Greenberg, P.D., and Hingorani, S.R. (2014). Targeted depletion of an MDSC subset unmasks pancreatic ductal adenocarcinoma to adaptive immunity. *Gut* *63*, 1769–1781.

Stromnes, I.M., Hulbert, A., Pierce, R.H., Greenberg, P.D., and Hingorani, S.R. (2017). T-cell localization, activation, and clonal expansion in human pancreatic ductal adenocarcinoma. *Cancer Immunol. Res.* *5*, 978–991.

Stuart, T., Butler, A., Hoffman, P., Hafemeister, C., Papalexi, E., Mauck, W.M., Hao, Y., Stoeckius, M., Smibert, P., and Satija, R. (2019). Comprehensive integration of single-cell data. *Cell* *177*, 1888–1902.e21.

Szolek, A., Schubert, B., Mohr, C., Sturm, M., Feldhahn, M., and Kohlbacher, O. (2014). OptiType: precision HLA typing from next-generation sequencing data. *Bioinformatics* *30*, 3310–3316.

Tran, E., Ahmadzadeh, M., Lu, Y.C., Gros, A., Turcotte, S., Robbins, P.F., Gartner, J.J., Zheng, Z., Li, Y.F., Ray, S., et al. (2015). Immunogenicity of somatic mutations in human gastrointestinal cancers. *Science* *350*, 1387–1390.

VanDussen, K.L., Sonnek, N.M., and Stappenbeck, T.S. (2019). L-WRN conditioned medium for gastrointestinal epithelial stem cell culture shows replicable batch-to-batch activity levels across multiple research teams. *Stem Cell Res.* *37*, 101430.

Vonderheide, R.H. (2018). The immune revolution: a case for priming, not checkpoint. *Cancer Cell* *33*, 563–569.

Vonderheide, R.H. (2020). CD40 agonist antibodies in cancer immunotherapy. *Annu. Rev. Med.* *71*, 47–58.

Weese, D., Holtgrewe, M., and Reinert, K. (2012). RazerS 3: faster, fully sensitive read mapping. *Bioinformatics* *28*, 2592–2599.

Wells, D.K., van Buuren, M.M., Dang, K.K., Hubbard-Lucey, V.M., Sheehan, K.C.F., Campbell, K.M., Lamb, A., Ward, J.P., Sidney, J., Blazquez, A.B., et al. (2020). Key parameters of tumor epitope immunogenicity revealed through a consortium approach improve neoantigen prediction. *Cell* *183*, 818–834.e13.

Wherry, E.J., and Kurachi, M. (2015). Molecular and cellular insights into T cell exhaustion. *Nat. Rev. Immunol.* *15*, 486–499.

Winograd, R., Byrne, K.T., Evans, R.A., Odorizzi, P.M., Meyer, A.R.L.L., Bajor, D.L., Clendenin, C., Stanger, B.Z., Furth, E.E., Wherry, E.J., et al. (2015). Induction of T-cell immunity overcomes complete resistance to PD-1 and CTLA-4 blockade and improves survival in pancreatic carcinoma. *Cancer Immunol. Res.* *3*, 399–411.

Yamamoto, K., Venida, A., Yano, J., Biancur, D.E., Kakiuchi, M., Gupta, S., Sohn, A.S.W., Mukhopadhyay, S., Lin, E.Y., Parker, S.J., et al. (2020). Autophagy promotes immune evasion of pancreatic cancer by degrading MHC-I. *Nature* *581*, 100–105.

Yarchoan, M., Albacker, L.A., Hopkins, A.C., Montesin, M., Murugesan, K., Vithayathil, T.T., Zaidi, N., Azad, N.S., Laheru, D.A., Frampton, G.M., et al. (2019). PD-L1 expression and tumor mutational burden are independent biomarkers in most cancers. *JCI Insight* *4*, e126908.

Yu, X., Harden, K., Gonzalez, L.C., Francesco, M., Chiang, E., Irving, B., Tom, I., Ivelja, S., Refino, C.J., Clark, H., et al. (2009). The surface protein TIGIT suppresses T cell activation by promoting the generation of mature immunoregulatory dendritic cells. *Nat. Immunol.* *10*, 48–57.

Zheng, G.X.Y., Terry, J.M., Belgrader, P., Ryvkin, P., Bent, Z.W., Wilson, R., Zivaldo, S.B., Wheeler, T.D., McDermott, G.P., Zhu, J., et al. (2017). Massively parallel digital transcriptional profiling of single cells. *Nat. Commun.* *8*, 14049.

STAR★METHODS

KEY RESOURCES TABLE

REAGENT or RESOURCE	SOURCE	IDENTIFIER
Antibodies		
<i>In vivo</i> mAb TIGIT antagonist	Absolute Antibody	1B4 Cat# Ab01258-1.1
<i>In vivo</i> mAb PD-1 antagonist	BioXCell	29F.1A12 Cat # BE0273 RRID:AB_2687796
<i>In vivo</i> mAb CD40 agonist	BioXCell	FGK4.5/FGK45 Cat# BE0016-2 RRID:AB_1107647
<i>In vivo</i> mAb Rat IgG2a isotype control	BioXCell	2A3 Cat# BE0089 RRID:AB_1107769
<i>In vivo</i> mAb Mouse IgG1 isotype control	BioXCell	MOPC-21 Cat# BE0083 RRID:AB_1107784
<i>In vivo</i> mAb CD8a	BioXCell	2.43 Cat# BP0061 RRID:AB_1125541
<i>In vivo</i> mAb TIGIT agonist	BioXCell	1G9 Cat # BE0274 RRID:AB_2687797
FC: anti-Human CD3	BD Biosciences	UCHT1 Cat# 612896; RRID: AB_2870184
FC: anti-Human CD8	BD Biosciences	SK1 Cat# 612755; RRID: AB_2870086
FC: anti-Human CD45RO	BD Biosciences	UCHL1 Cat# 564292; RRID: AB_2744410
FC: anti-Human CD57	BD Biosciences	HNK-1 Cat# 359621; RRID: AB_2565929
FC: anti-Human HLA-DR	BD Biosciences	G46-6 Cat# 612981; RRID: AB_2870252
FC: anti-Human/Mouse Ki67	BD Biosciences	B56 Cat# 563756; RRID: AB_2732007
FC: anti-Human LAG3	BioLegend	11C3c65 Cat# 369331; RRID: AB_2734421
FC: anti-Human PD-1	BD Biosciences	EH12.1 Cat# 563076; RRID: AB_2737990
FC: anti-Human/Mouse TCF-1	Cell Signaling Technologies	C63D9 Cat# 6709S; RRID: AB_2797631
FC: anti-Human TIGIT	Invitrogen	MBSA43 Cat# 25-9500-41; RRID: AB_2573547
FC: anti-Human TIM3	BD Biosciences	7D3 Cat# 565567; RRID: AB_2744370
FC: anti-Mouse CD4	BioLegend	RM4-5 Cat# 100530; RRID: AB_389325
FC: anti-Mouse CD4	BD Biosciences	RM4-6 Cat# 612843; RRID: AB_2870165
FC: anti-Mouse CD8a	BD Biosciences	53-6.7 Cat# 563786; RRID: AB_2732919

(Continued on next page)

Continued

REAGENT or RESOURCE	SOURCE	IDENTIFIER
FC: anti-Mouse CD8a	BioLegend	53-6.7 Cat# 100738; RRID: AB_11204079
FC: anti-Mouse CD8a	BioLegend	53-6.7 Cat# 100701; RRID: AB_312740
FC: anti-Mouse CD44	BioLegend	IM7 Cat# 103047; RRID: AB_2562451
FC: anti-Mouse CD44	BioLegend	IM7 Cat# 103057; RRID: AB_2564214
FC: anti-Mouse CD44	Invitrogen	IM7 Cat# 11-0441-82; RRID: AB_465045
FC: anti-Mouse CD45	Invitrogen	30-F11 Cat# 47-0451-82; RRID: AB_1548781
FC: anti-Mouse CD45	BioLegend	30-F11 Cat# 103149; RRID: AB_2564590
FC: anti-Mouse EpCam	BioLegend	G8.8 Cat# 118216; RRID: AB_1236471
FC: anti-Mouse H-2Db	Invitrogen	28-14-8 Cat# 11-5999-82; RRID: AB_465361
FC: anti-Mouse H-2Kb	BioLegend	AF6-88.5 Cat# 116518; RRID: AB_10564404
FC: anti-Mouse Ki67	BD Biosciences	B56 Cat# 563756; RRID: AB_2732007
FC: anti-Mouse Ki67	BD Biosciences	B56 Cat# 561277; RRID: AB_10611571
FC: anti-Mouse LAG3	Invitrogen	C9B7W Cat# 11-2231-82; RRID: AB_2572484
FC: anti-Mouse MHC-II (I/A-I/E)	BioLegend	M5/114.15.2 Cat# 107643; RRID: AB_2565976
FC: anti-Mouse PD-1	BioLegend	29F.1A12 Cat# 135241; RRID: AB_2715761
FC: anti-Mouse PD-L1	BioLegend	10F.9G2 Cat# 124315; RRID: AB_10897097
FC: anti-Mouse PD-L1	BioLegend	10F.9G2 Cat# 124312; RRID: AB_10612741
FC: anti-Mouse TIGIT	Invitrogen	GIGD7 Cat# 46-9501-82; RRID: AB_11150967
FC: anti-Mouse TIM3	BioLegend	RMT3-23 Cat# 119721; RRID: AB_2616907
FC: anti-Mouse CD172a	BioLegend	P84 Cat# 144006; RRID: AB_11204425
FC: anti-Mouse XCR1	BioLegend	ZET Cat# 148204; RRID: AB_2563843
FC: anti-Mouse CD11c	eBioscience	N418 Cat# 25-0114-81; RRID: AB_469589
FC: anti-Mouse B220	BioLegend	RA3-6B2 Cat# 103258; RRID: AB_2564053
FC: anti-Mouse Ly-6C	BioLegend	HK1.4 Cat# 128012; RRID: AB_1659241
FC: anti-Mouse PD-L1	BioLegend	10F.9G2 Cat# 124321; RRID: AB_2563635
FC: anti-Mouse CD11b	BioLegend	M1/70 Cat# 101243; RRID: AB_2561373
FC: anti-Mouse F4/80	BioLegend	RA3-6B2 Cat# 123116; RRID: AB_893481

(Continued on next page)

Continued

REAGENT or RESOURCE	SOURCE	IDENTIFIER
FC: anti-Mouse Ly-6G	BioLegend	1A8 Cat# 127622; RRID: AB_10643269
FC: anti-Human PVR/CD155	BD Biosciences	Tx24 Cat# 744880; RRID: AB_2742557
FC: anti-Mouse CD155	BD Biosciences	Tx56 Cat# 748221; RRID: AB_2872652
FC: anti-Mouse CD155	BD Biosciences	3F1 Cat# 743256; RRID: AB_2741379
IHC: anti-Mouse CD4	Abcam	EPR19514 Cat# ab183685; RRID: AB_2686917
IHC: anti-Mouse CD8	Abcam	EPR21769 Cat# ab217344; RRID: AB_2890649
mIHC: anti-Mouse CD8-AF647	Abcam	EPR21769 Cat# ab237365
IHC: anti-Mouse CK19	DHSB	Troma-III N/A; RRID: AB_2133570
IHC: anti-RFP	Rockland	Cat# 600-401-379; RRID: AB_2209751
IHC: anti-Human CD155/PVR	Abcam	EPR22672-151 Cat# ab267788
IHC: anti-Mouse CD155/PVR	LSBio	Cat# LS-B12331
IHC: anti-Mouse CD155/PVR	LSBio	Cat# LS-C376428
IHC: anti-Mouse CD155/PVR	LSBio	Cat# Ab233102
IHC: anti-Mouse PD-L1	LSBio	Cat# LS-C746930
IHC: anti-Mouse Galectin-9	LSBio	Cat# LS-B6275; RRID: AB_11045131
IHC: anti-Mouse anti-smooth muscle actin	Abcam	Cat# ab5694; RRID: AB_2223021

Bacterial and Virus Strains

Adenovirus (Ad-CMV-Cre)	Viral Vector Core, University of Iowa	Ad5-CMV-Cre
One Shot Stbl3 chemically competent <i>E. coli</i>	Thermo Fisher Scientific	Cat# C7373-03

Biological Samples

Human pancreatic cancer tumor microarray	BioMax	Cat# PA1002b
Human pancreatic cancer biospecimens	This manuscript	Massachusetts General Hospital; Collected under IRB# P001858
Human healthy peripheral blood mononuclear cells	StemCell	Cat# 70025.1
Human pancreatic cancer organoids	This manuscript	Massachusetts General Hospital; Collected under IRB# P001858

Chemicals, Peptides, and Recombinant Proteins

Recombinant human IL-2	Peptotech	Cat# AF-200-02
B-27	Invitrogen	Cat# 17504044
N-acetylcysteine	Sigma-Aldrich	Cat# A9165
Nicotinamide	Sigma-Aldrich	Cat# N0636
EGF	Novus Biologicals	Cat# NBP2-34952
A 83-01	Cayman Chemical	Cat# 9001799
SB 202190	Cayman Chemical	Cat# 10010399
PGE2	Cayman Chemical	Cat# 14010
Nutlin-3a	Sigma-Aldrich	Cat# SML0580
OVA (257 - 264); SIINFEKL peptide	Anaspec	Cat# AS-60193-1
Recombinant murine interferon-gamma (IFN γ)	Peptotech	Cat# 315-05

(Continued on next page)

Continued

REAGENT or RESOURCE	SOURCE	IDENTIFIER
Recombinant mouse leukemia inhibitory factor (mLIF)	Amsbio	Cat# AMS-263-100
CHIR-99021	AbMole	Cat# M1692
PD-0325901	AbMole	Cat# M1763
Collagenase, Type 4	Worthington	Cat# LS004189
Corning® Matrigel® Growth Factor Reduced (GFR) Basement Membrane Matrix, Phenol Red-free	Corning	Cat# 356231
TrypLE Express	Life Technologies	Cat# 12604-013
FastDigest Esp3I	Thermo Fisher	Cat# FD0454
UltraComp eBeads™ Compensation Beads	Thermo Fisher	Cat# 01-2222-42
Tris-EDTA pH 9	Abcam	Cat# ab93684
H-2K(b) 257-264 SIINFEKL monomer	NIH Tetramer Core Facility	N/A
H-2K(b) mouse mAlg8 503-510 ITYTWTRL monomer	NIH Tetramer Core Facility	N/A
H-2K(b) mouse mLama4 1254-1261 VGFNFRTL monomer	NIH Tetramer Core Facility	N/A

Critical Commercial Assays

GeoMx Solid Tumor Morphology Kit (Mouse)	Nanostring	Cat# 121300304
GeoMx Immune Cell Profiling (Mouse)	Nanostring	Cat# 121300106
GeoMx IO Drug Target (Mouse)	Nanostring	Cat# 121300107
GeoMx Immune Activation Status (Mouse)	Nanostring	Cat# 121300117
GeoMx Immune Cell Type (Mouse)	Nanostring	Cat# 121300118
GeoMx Protein Slide Prep FFPE	Nanostring	Cat# 121300312
GeoMx Hybridization Code Pack (Protein)	Nanostring	Cat# 121300401
GeoMx Master Kit	Nanostring	Cat# 100052
GeoMx DSP Collection Plate	Nanostring	Cat# 100473

Deposited Data

Murine scRNA-seq data	This manuscript	GEO accession#: GSE163059
Human scRNA-seq data	Peng et al. (2019)	Genome Sequencing Archive; CRA001160
TCGA (PAAD, COAD, LUAD) RNA-seq	The Cancer Genome Atlas Research Network (TCGA)	gdac.broadinstitute.org
TCGA (PAAD) WES	The Cancer Genome Atlas Research Network (TCGA)	gdac.broadinstitute.org
PancSeq WES/RNA-seq	Aguirre et al. (2018)	dbGaP; phs001652.v1.p1

Experimental Models: Cell Lines

KP*1 mESC line	This manuscript	N/A
Organoid lines, see Table S3	This manuscript	N/A
L-WRN cell line	ATCC	Cat# CRL-3276
Cultrex HA-R-Spondin1-Fc 293T cell line	Trevigen	Cat# 3710-001-K
Leading Light Wnt reporter cell line	Enzo	Cat# ENZ-61002
Green-Go	Sánchez-Rivera et al. (2014)	N/A

Experimental Models: Organisms/Strains

<i>C57BL/6J-KP; Rosa26^{CAG-LSL-dCas9-VPR-P2A-mNeonGreen}</i>	This manuscript	N/A
<i>C57BL/6-Tg(TcraTcrb)1100Mjb/J (OT-I)</i>	Jackson Laboratory	Cat# 003831
<i>C57BL/6-Rag2^{tm1.1Cgn}/J (Rag2^{-/-})</i>	Jackson Laboratory	Cat# 008449
<i>C57BL/6J-Kras^{LSL-G12D/+}; Trp53^{fllox/fllox} (KP)</i>	Jackson et al. (2001) ; Marino et al. (2000)	N/A
<i>C57BL/6J</i>	Jackson Laboratory	Cat# 000664

(Continued on next page)

Continued

REAGENT or RESOURCE	SOURCE	IDENTIFIER
Oligonucleotides		
CRISPRa sgRNAs, see Table S5	This manuscript	N/A
CRISPR-KO sgRNAs, see Table S5	This manuscript	N/A
Recombinant DNA		
Hipp11-mScarletSIIN targeting vector	This manuscript	N/A
Hipp11-mScarletmLAMA4 targeting vector	This manuscript	N/A
Hipp11-mScarletmALG8 targeting vector	This manuscript	N/A
Rosa26-dCas9-VPR-mNG targeting vector	This manuscript	N/A
U6-sgfiller-eCas9-T2A-BlastR	This manuscript	N/A
U6-sgH11.1-eCas9-T2A-BlastR	This manuscript	N/A
U6-sgR26.1-eCas9-T2A-BlastR	This manuscript	N/A
LV-PGK-Cre	This manuscript	N/A
LV-PGK-Cre-EFS-mScarletSIIN	This manuscript	N/A
LV-PGK-PVR-P2A-Cre-EFS-mScarletSIIN	This manuscript	N/A
LV-U6-sgRNAfiller-PGK-Cre-EFS-mScarletSIIN	This manuscript	N/A
LV-U6-sgNT-PGK-Cre-EFS-mScarletSIIN	This manuscript	N/A
LV-U6-sgPvra.1-PGK-Cre-EFS-mScarletSIIN	This manuscript	N/A
LV-U6-sgPvra.2-PGK-Cre-EFS-mScarletSIIN	This manuscript	N/A
PsPax2	Addgene	Cat# 12260; RRID: Addgene_12260
Pmd2.G	Addgene	Cat# 12259; RRID: Addgene_12259
SP-dCas9-VPR	Addgene	Cat# 63798; RRID: Addgene_63798
Software and Algorithms		
Vevo Lab software	Fujifilm-Visualsonics	N/A
Flowjo v10 software	BD Biosciences	N/A
GraphPad Prism 9	GraphPad	N/A
QuPath	Bankhead et al. (2017)	N/A
R	The R Project for Statistical Computing	R-project.org
cBioPortal	The cBioPortal for Cancer Genomics	cbioportal.org
OptiType	Szolek et al. (2014)	https://github.com/FRED-2/OptiType
seq2hla	Boegel et al., 2012	https://github.com/TRON-Bioinformatics/seq2HLA
Samtools	Li et al. (2009)	http://samtools.sourceforge.net
RazerS 3	Weese et al. (2012)	https://www.seqan.de/apps/razers-3/
Strelka2	Kim et al. (2018)	https://github.com/Illumina/strelka
Scalpel	Narzisi et al. (2014)	http://scalpel.sourceforge.net
Manta	Chen et al. (2016)	https://github.com/Illumina/manta
UCSC genome browser	Haeussler et al. (2019)	https://genome.ucsc.edu/util.html
Picard	NA	http://broadinstitute.github.io/picard/
VCFtools	Danecek et al. (2011)	https://vcftools.github.io/index.html
Ensemble Variant Effect Predictor	McLaren et al. (2016)	https://uswest.ensembl.org/info/docs/tools/vep/index.html
pVACtools	Hundal et al. (2020)	https://pvactools.readthedocs.io/en/latest/
NetMHC-4.0	Andreatta and Nielsen (2016)	http://tools.iedb.org/mhci/
NetMHCpan-4.0	Jurtz et al. (2017)	http://tools.iedb.org/mhci/
SMM	Kim et al. (2009)	http://tools.iedb.org/mhci/
SMMPMBEC	Peters and Sette (2005)	http://tools.iedb.org/mhci/

(Continued on next page)

Continued

REAGENT or RESOURCE	SOURCE	IDENTIFIER
Cell Ranger	10x Genomics	https://github.com/10XGenomics/cellranger
Seurat	Butler et al. (2018)	https://satijalab.org/seurat/install.html
SCDE	Fan et al. (2016)	https://github.com/hms-dbmi/scde
biomaRt	Durinck et al. (2005), 2009	https://github.com/grimbough/biomaRt
scRNA-seq analysis code	This manuscript	https://github.com/Zack-Ely/PDAC-Cancer-Cell
Neopeptide prediction code	This manuscript	https://github.com/Zack-Ely/PDAC-Cancer-Cell

Other

Vevo3100/LAZRX ultrasound and photoacoustic imaging system	Fujifilm-Visualsonics	N/A
GeoMx Digital Spatial Profiler	Nanostring	N/A
Incucyte S3	Sartorius	N/A
gentleMACS™ Octo Dissociator	Miltenyi Biotec	Cat# 130-095-937
LSR II HTS-2	BD Biosciences	N/A
LSR Fortessa	BD Biosciences	N/A
Aria IIIu sorter	BD Biosciences	N/A
whole_exome_agilent_1.1_refseq_plus_3_boosters.targetIntervals.bed	Agilent/UCSC	https://cghub.ucsc.edu

RESOURCE AVAILABILITY

Lead contact

Further information and requests for resources and reagents should be directed to and will be fulfilled by the lead contact, Tyler Jacks (tjacks@mit.edu).

add Materials availability

Plasmids generated in this study have been deposited to Addgene. Mouse lines and organoid lines generated in this study will made available to the broader scientific community upon request to the lead contact.

Data and code availability

The datasets generated and/or analyzed during the current study are available in the NCBI Gene Expression Omnibus (GEO) under accession number: GSE163059. Computer code for neopeptide predictions and scRNA-seq analysis available at <https://github.com/Zack-Ely/PDAC-Cancer-Cell>. Other software tools (including version numbers) for exome, RNA-seq, and scRNA-seq analyses are listed in the [Key resources table](#).

EXPERIMENTAL MODEL AND SUBJECT DETAILS

Mice

All animal studies described in this study were approved by the MIT Institutional Animal Care and Use Committee. All animals were maintained on a pure *C57BL/6J* genetic background. Generation of *Kras*^{LSL-G12D/+} and *Trp53*^{flox/flox} (KP) mice has previously been described (Jackson et al., 2001; Marino et al., 2000) and were bred in house. *OT-I* TCR transgenic mice have been previously described (Hogquist et al., 1994). *Rag2*^{-/-} mice have been previously described (Hao and Rajewsky, 2001). *OT-I* and *Rag2*^{-/-} mice were purchased from The Jackson Laboratory (JAX) or bred in house. *KP; Rosa26*^{CAG-LSL-dCas9-VPR-P2A-mNeonGreen} mice were generated as part of this study (described in detail below).

mESC generation and CRISPR-assisted targeting

“KP*1”, a *C57BL/6J Kras*^{LSL-G12D/+}; *Trp53*^{flox/flox} (KP) murine embryonic stem cell (mESC) line, was generated by crossing a hormone-primed *C57BL/6J Trp53*^{flox/flox} female with a *C57BL/6J Kras*^{LSL-G12D/+}; *Trp53*^{flox/flox} male. At 3.5 days post-coitum, blastocysts were flushed from the uterus, isolated, and cultured on a mouse embryonic fibroblast (MEF) feeder layer in ‘ESCM+LIF+2i’ [Knockout DMEM (Gibco), 15% FBS (Hyclone), 1% NEAA (Sigma), 2 mM Glutamine (Gibco), 0.1 mM β-mercaptoethanol (Sigma-Aldrich) 50 IU Penicillin, 50 IU Streptomycin, 1000 U/ml LIF (Amsbio), 3 μM CHIR99021 (AbMole), 1 μM PD0325901 (AbMole)]. After 5-7 days in culture the outgrown inner cell mass was isolated, trypsinized and re-plated on a fresh MEF layer. ES cell lines were genotyped

for *Kras*^{LSL-G12D/+}, *Trp53*^{flox/flox}, and *Zfy* (Y-chromosome specific). Primer sequences available upon request. ES cell lines were tested for pluripotency by injection into host blastocysts from albino mice to generate chimeric mice.

DNA mixes (1:1 mix of 'U6-sgH11-eCas9-T2A-BlastR' + 'H11-targeting vector' [H11-mScarletSIIN, H11-mScarletLAMA4, or H11-mScarletALG8]) or 1:1 mix of 'U6-sgR26-eCas9-T2A-BlastR' + 'R26-dCas9-VPR targeting vector') were ethanol precipitated prior to DNA (1 μ g) transfection of approximately 3×10^5 KP*1 mESCs in a gelatin-coated 24-well plate using Lipofectamine 2000 (Thermo Fisher) according to the manufacturer instructions. mESCs were selected with Blasticidin (6 μ g/mL) for 2 days, starting 36 hours post-transfection, prior to low-density re-plating on MEF feeder lines in absence of Blasticidin. Large mESC colonies were manually picked using a stereomicroscope, expanded and evaluated for correct integration using PCR with primers spanning both the 5' and 3' homology arms (primer sequences available on request). Correct clones by PCR evaluation were evaluated using Southern blot analysis. Briefly, genomic DNA was digested overnight with NsiI-HF (for H11-mScarletSIIN targeting) or PacI (for R26-dCas9-VPR targeting). Digestions were electrophoresed on 0.7% agarose gels and blotted to Amersham Hybond XL nylon membranes (GE Healthcare). Samples were probed with 32P-labeled 5' external, 3' external, and internal probes applied in Church buffer (Church and Gilbert, 1984) (probe sequences available on request).

Correctly targeted clones were injected into albino *C57BL/6J* blastocysts. Chimerism was assessed by coat color. Pancreatic organoids were isolated from chimeric animals and "donor" organoids were purified from the host pancreas using 72 hours of Puromycin (6 μ g/mL) selection (leveraging the presence of the Puromycin resistance gene within the LSL cassette upstream of *Kras-G12D*) (Jackson et al., 2001).

Organoid generation and characterization

Pancreatic organoid isolation and propagation has been previously described (Boj et al., 2015). Briefly, for genetically-defined pancreatic organoids, pancreata were manually dissected from genetically-engineered mice of the desired genotype. Pancreata were then manually minced with razor blades and dissociated in pancreas digestion buffer [1x PBS, 125 U/mL collagenase IV (Worthington)] for 20 minutes at 37°C. Cell suspensions were filtered through 70 μ m filters, washed with 1x PBS and centrifuged with slow deceleration. Cell pellets were resuspended in 100% growth-factor reduced Matrigel (Corning) and solidified at 37°C. Cells were subsequently cultured in organoid complete media (minor modifications from previously described formulations (Boj et al., 2015) (see details below) and monitored for organoid outgrowth. Organoids were passaged with TrypLE Express (Life Technologies) for at least 4 passages to purify the ductal component prior to Cre recombinase-mediated recombination. For recombination, organoids were spininfected with adenoviral (Ad5-CMV-Cre) at a MOI >100 to ensure 100% recombination. All organoids were authenticated by genotyping at *Kras* and *Trp53* loci both prior to and following Ad-CMV-Cre to ensure proper recombination. See Table S3 for details on organoid lines.

Murine and human tumor-derived organoids were isolated following the same procedure as above with the exception of 30 minutes in pancreas digestion buffer. Tumor-derived organoids were passaged at least four times prior to experimental manipulation to remove contaminating cell types. Murine tumor-derived organoids were selected via resistance to Nutlin-3a (10 μ M, Sigma-Aldrich) to ensure purification of the malignant compartment. Pancreatic organoids were maintained in culture for <20 passages.

Media for pancreatic organoids was formulated based on L-WRN cell conditioned media (L-WRN CM) (VanDussen et al., 2019). Briefly, L-WRN CM was generated by collecting 8 days of supernatant from L-WRN cells, grown in Advanced DMEM/F12 (Gibco) supplemented with 20% fetal bovine serum (Hyclone), 2 mM GlutaMAX, 100 U/mL of penicillin, 100 μ g/mL of streptomycin, and 0.25 μ g/mL amphotericin. L-WRN CM was diluted 1:1 in Advanced DMEM/F12 (Gibco) and supplemented with additional RSP0-1 conditioned media (10% v/v), generated using Cultrex HA-R-Spondin1-Fc 293T Cells. The following molecules were also added to the growth media: B27 (Gibco), 1 μ M N-acetylcysteine (Sigma-Aldrich), 10 μ M nicotinamide (Sigma-Aldrich), 50 ng/mL EGF (Novus Biologicals), 500 nM A83-01 (Cayman Chemical), 10 μ M SB202190 (Cayman Chemical), and 500 nM PGE2 (Cayman Chemical). Wnt activity of the conditioned media was assessed and normalized between batches via luciferase reporter activity of TCF/LEF activation (Enzo Leading Light Wnt reporter cell line).

T cell culture

OT-I splenocytes were harvested from *C57BL/6J OT-I* transgenic mice, and spleens were mashed through 70 μ m filters. Red blood cells were lysed with ACK buffer for 2 min before cell suspension neutralization with PBS and pelleted for plating. Splenocytes were counted and adjusted to 1×10^6 cells/mL in T cell medium [RPMI 1640 (Corning) supplemented with 10% heat-inactivated FBS, 20 mM HEPES (Gibco), 1 mM Sodium Pyruvate (Thermo Fisher), 2 mM L-Glutamine (Gibco), 50 μ M β -mercaptoethanol (Gibco), 1X Non-Essential Amino Acids (Sigma), 0.5X Pen/Strep (Gibco) with 10 ng/mL hIL-2 (Peprotech) and 1 μ M SIINFEKL peptide (Anaspec)]. Splenocytes were activated for 24h at 37°C in a tissue culture incubator, before manual CD8 α isolation according to manufacturer instructions (Milteny Biotec). OT-I T cells were subsequently expanded 4-6 days in T cell medium with 10 ng/mL hIL-2 prior to organoid co-culture.

Organoid + CD8 T cell co-culture

Pancreatic organoids were dissociated using TrypLE Express (Life Technologies) and single cell suspensions were generated by vigorous resuspension. Activated OT-I CD8⁺ T cells (see above) and organoid cell numbers were determined by manual hemocytometer cell counting, and T cells + organoids were mixed at defined effector:target (E:T) ratios. Matrigel was then added (5 μ L per well in black-walled 96-well plates (Corning) for Incucyte live cell imaging; 20-50 μ L per well for culture in 24-well plates; final 85% Matrigel)

before solidification at 37°C. Cells were cultured in complete organoid medium supplemented with 10 ng/mL hIL-2 (Peprotech). Incucyte images of co-cultures were acquired every 4 hours (Brightfield and RFP channels) for 6–10 days for Incucyte live cell imaging or imaged at Day 5–7 for larger cultures.

Orthotopic transplantation

Orthotopic transplantation of organoids was performed with minor modifications to previously reported protocols for orthotopic transplantation of pancreatic monolayer cell lines (Kim et al., 2009). Briefly, animals were anesthetized using Isoflurane, the left subcostal region was depilated (using clippers or Nair) and the surgical area was disinfected with alternating Betadine/Isopropyl alcohol. A small (~2 cm) skin incision was made in the left subcostal area and the spleen was visualized through the peritoneum. A small incision (~2 cm) was made through the peritoneum overlying the spleen and the spleen and pancreas were exteriorized using ring forceps. A 30-gauge needle was inserted into the pancreatic parenchyma parallel to the main pancreatic artery and 100 μ L (containing 1.25×10^5 organoid cells in 50% PBS + 50% Matrigel) was injected into the pancreatic parenchyma. Successful injection was visualized by formation of a fluid-filled region within the pancreatic parenchyma without leakage. The pancreas/spleen were gently interlaced and the peritoneal and skin layers were sutured independently using 5-0 vicryl sutures. All mice received pre-operative analgesia with Bup-SR and were followed post-operatively for any signs of discomfort or distress. Organoid/Matrigel mixes were kept on ice throughout the entirety of the procedure to prevent solidification prior to injection. For orthotopic transplantation, syngeneic C57BL/6J mice (aged 4–12 weeks) were transplanted. Male pancreatic organoids were only transplanted back into male recipients.

Small rodent ultrasound

Quantification of murine pancreatic tumors by high resolution ultrasound has been previously described (Sastra and Olive, 2013). Briefly, animals were anesthetized using Isoflurane and the lateral and ventral abdominal areas were depilated using Nair. Sterile 0.9% saline (1 mL) was administered by i.p. injection prior to imaging to improve visualization of the pancreas. Animals were imaged using the Vevo3100/LAZRX ultrasound and photoacoustic imaging system (Fujifilm-Visualsonics). Animals were placed on the imaging platform in the supine position and a layer of ultrasound gel was applied over the entirety of the abdominal area. The ultrasound transducer (VisualSonics 550S) was placed on the abdomen orthogonal to the plane of the imaging platform. Landmark organs, such as the kidney, spleen, and liver, were identified in order to define the area of the pancreas. The transducer was set at the scanning midpoint of the normal pancreas or pancreatic tumor and a 3D image of 10–20 mm, depending on tumor size, at a Z-slice thickness of 0.04 mm. 3D images were uploaded to the Vevo Lab Software. The volumetric analysis function was used to define the tumor border at various Z-slices through the entirety of the tumor and derive the final calculated tumor volume.

Preclinical trials

Age- and sex-matched recipient C57BL/6J mice were purchased from The Jackson Laboratory (JAX) or bred in house. Orthotopic transplantation was performed as described above. Mice were monitored for tumor development at 4, 5, 6 weeks post-initiation using high-resolution ultrasound (as described above) to confirm tumor establishment and interval growth. Animals with established tumors (baseline 10–220 mm³ by 6 weeks post-initiation; median 68 mm³) were randomized by tumor burden within 24 hours of baseline imaging to either control or experimental treatment arms. Researchers performing health checks, ultrasound imaging and interpretation were blinded to cohort allocation. Isotype (control) arm consisted of 200 μ g/mouse Rat IgG2a (BioXCell) + 100 μ g/mouse Mouse IgG1 (BioXCell). Experimental arms consisted of anti-PD-1 (Liang et al., 2003) (BioXCell; Clone 29F.1A12; Rat IgG2a; 200 μ g/mouse, dosed i.p. every 2–3 days), anti-TIGIT (Dixon et al., 2018) (Absolute Antibody; Clone 1B4; Mouse IgG1; 100 μ g/mouse, dosed i.p. every 2–3 days), CD40 agonist (Roliink et al., 1996) (BioXCell; Clone FGK4.5/FGK45; Rat IgG2a; 100 μ g/mouse, dosed i.p. once every 4 weeks) monotherapy or combination therapy as described in the text. Animals were treated for 4 weeks and weekly weights and ultrasound imaging was performed as described. Tumor response was assessed on all evaluable animals at time points (t) >10 days using modified RECIST (mRECIST) criteria, previously adapted for volumetric imaging and preclinical testing (Gao et al., 2015). Briefly, tumor volume (V) at each time point (t) was compared to the baseline tumor volume (V_{baseline}) in a given animal: (percent change) $\Delta Vol_t = (V_t - V_{\text{baseline}}) / V_{\text{baseline}} * 100\%$. For each animal, we calculated both a “BestResponse” (defined as the minimum ΔVol_t for $t > 10$ days) and “BestAvgResponse” (defined as the minimum average for $t > 10$ days, where for each time point (t), the average ΔVol_t reflects that time point’s ΔVol_t and all prior ΔVol_t). Modified RECIST (mRECIST) criteria were defined as: mCR = BestResponse < –95% and BestAvgResponse < –40%; mPR = BestResponse < –50% and BestAvgResponse < –20%; mSD = BestResponse < 35% and BestAvgResponse < 30%; mPD = not otherwise specified. See (Gao et al., 2015) for full details on mRECIST derivation and validation.

Retrograde pancreatic duct delivery

Retrograde pancreatic duct instillation of lentivirus has been previously described (Chiou et al., 2015). We adapted this technique in a number of ways. Briefly, the ventral abdomen was depilated (using clippers or Nair) 1–2 days prior to surgery. Animals were anesthetized with Isoflurane and the surgical area was disinfected with alternating Betadine/Isopropyl alcohol. A small skin incision was made in the anterior abdomen (~2–3 cm midline incision extending caudally from the xiphoid process). A subsequent incision was made through the linea alba and incision edges were secured in place with a Colibri retractor. The remainder of the procedure was conducted under a Nikon stereomicroscope. A moistened (with sterile 0.9% saline) sterile cotton swab was used to gently move the left lobe of the liver cranially towards the diaphragm. A second moistened sterile cotton swab was used to gently reposition the

colon/small intestine into the right lower abdominal quadrant, until the duodenum was visualized. The duodenum was gently repositioned (still in the abdominal cavity) using moistened cotton swabs until the pancreas, common bile duct and sphincter of Oddi were well visualized. The common bile duct and cystic duct were gently separated from the portal vein and hepatic artery using blunt dissection with Moria forceps. A microclip was placed over the common bile duct (cranial to pancreatic duct branching) to prevent influx of the viral particles into the liver or gallbladder, forcing the viral vector retrograde through the pancreatic duct. To infuse the viral vector, the common bile duct was cannulated with a 30-gauge needle at the level of the sphincter of Oddi and 150 μ L of virus was injected over the course of 30 seconds. Gentle pressure was applied at the sphincter of Oddi upon needle exit to prevent leakage into the abdominal cavity. Subsequently, the microclip and Colibri retractor were removed. The peritoneum was closed using running 5-0 Vicryl sutures. The cutis and fascia were closed using simple interrupted 5-0 Vicryl sutures. The entire procedure was conducted on a circulating warm water heating blanket to prevent intra-operative hypothermia. All mice received pre-operative analgesia with sustained-release Buprenorphine (Bup-SR) and were followed post-operatively for any signs of discomfort or distress. For retrograde pancreatic ductal installation, male mice (aged 3-6 weeks) and female mice (aged 3-8 weeks) were transduced with 250,000 TU (transducing units, see viral titering) in serum-free media (Opti-MEM; Gibco).

Consistent with prior reports using retrograde pancreatic duct delivery of Cre-containing lentivirus (Chiou et al., 2015), we observed that 17-24% of animals developed small soft tissue sarcomas (most frequently near the abdominal wall incision site) in addition to development of PanIN/PDAC in the pancreas, but these were easily discernable from pancreatic tumors.

For experiments involving CD8 depletion, animals were dosed with CD8 α depleting antibody (BioXCell, Clone 2.43, 200 μ g/mouse, dosed intraperitoneally [i.p.] every 3-4 days) beginning one day prior to surgery. For TIGIT agonist experiments, animals were dosed with TIGIT agonistic mAb (BioXCell, Clone 1G9, Mouse IgG1, 100 μ g/mouse, dosed intraperitoneally [i.p.] every 2-3 days) or Mouse IgG1 isotype control Ab (BioXCell, 100 μ g/mouse, dosed intraperitoneally [i.p.] every 2-3 days) beginning one day after surgery.

METHOD DETAILS

Molecular cloning

H11-mScarletSIIN, H11-mScarletLAMA4, and H11-mScarletALG8 targeting vectors were generated using gBlocks (IDT) and Gibson assembly (Akama-Garren et al., 2016; Gibson et al., 2009). In H11-mScarletSIIN, SIINFEKL was flanked by 17 amino acids on its N-terminus and 9 amino acids on its C-terminus to ensure antigen processing. mLAMA4 and mALG8 neoantigens were each preceded by 4 amino acids from their respective genes to ensure antigen processing. SP-dCas9-VPR was a gift from George Church (Addgene plasmid # 63798 ; <http://n2t.net/addgene:63798> ; RRID:Addgene_63798). R26-dCas9-VPR-mNG was cloned using a combination of PCR (to generate dCas9-VPR) and gBlocks (IDT) and Gibson assembly. U6-sgfiller-eCas9-T2A-BlastR was generated using Gibson assembly. In order to insert sgRNAs, the vector was digested with FastDigest Esp3I (Thermo Fisher) and ligated with BsmBI-compatible annealed oligonucleotides. sgRNAs targeting *Hipp11* or *Rosa26* were designed using Benchling (www.benchling.com), which was also used to predict potential off-target sites.

Lentiviral vectors (LV-PGK-Cre, LV-PGK-Cre-EFS-mScarletSIIN, LV-PGK-PVR-P2A-Cre-EFS-mScarletSIIN, LV-U6-sgRNAfiller-PGK-Cre-EFS-mScarletSIIN) were generated using Gibson assembly. In order to insert sgRNAs into LV-U6-sgRNAfiller-PGK-Cre-EFS-mScarletSIIN, the vector was digested with FastDigest Esp3I (Thermo Fisher) and ligated with BsmBI-compatible annealed oligonucleotides. CRISPRa-compatible sgRNAs targeting *Pvr* were adapted from (Horlbeck et al., 2016). See Table S5 for sgRNA and oligonucleotide sequences. All vectors with detailed maps and sequences have been deposited into Addgene.

Lentiviral production/titering

Lentiviral plasmids and packaging vectors were prepared using endotoxin-free maxiprep kits (QIAGEN). Lentiviruses were produced by co-transfection of HEK293 cells with lentiviral constructs plus packaging vectors: PsPax2 (psPAX2 was a gift from Didier Trono - Addgene plasmid # 12260 ; <http://n2t.net/addgene:12260> ; RRID:Addgene_12260) and Pmd2.G (pMD2.G was a gift from Didier Trono - Addgene plasmid # 12259 ; <http://n2t.net/addgene:12259> ; RRID:Addgene_12259). Viral supernatant was harvested 48 and 72 hours post transfection, filtered through a 0.45 μ m low-protein binding PVDF filter (EMD Millipore), and concentrated by ultracentrifugation (25,000 rpm for 2 hours at 4°C). Concentrated virus was resuspended in Opti-MEM (Gibco) and lentiviral aliquots were frozen and stored at -80°C. Lentiviral titers were determined using Green-Go cells as previously described (Sánchez-Rivera et al., 2014).

Flow cytometry

Flow cytometry of pancreatic organoids

Pancreatic organoids were grown as described above. Where indicated, organoids were treated with interferon-gamma (10 ng/mL; PeproTech) for 48-72 hours prior to analysis. Organoids were dissociated using TrypLE (15 minutes to minimize cleavage of surface proteins) washed with PBS, and filtered through 70 μ m filters. Single cell suspensions were pelleted at 2000 rpm and transferred to 96-well round-bottom plates for flow cytometric staining. Prior to surface staining, cell pellets were resuspended in Live/Dead dye (Ghost Dye Red 780, Tonbo Biosciences) diluted 1:1000 in PBS on ice for 20 minutes in the dark. Surface staining was performed on cells in PBS with 1% heat-inactivated FBS on ice for 30 min in the dark. Antibody information in Table S4.

Flow cytometry of murine PDAC

Tumors/pancreata were collected in RPMI 1640 supplemented with 1% heat-inactivated FBS. Tumors were finely minced with scissors in MACS C tubes (Miltenyi Biotec), and digested for 30 minutes at 37°C with gentle agitation in 5 mL digestion buffer [1x HBSS (Gibco), 1 mM HEPES (Gibco), 1% heat-inactivated FBS, 125 U/mL collagenase IV (Worthington), 40 U/mL DNase I, grade II (Roche)]. Pancreas tumors were processed on a gentleMACS Octo Dissociator using the “m_spleen_04” program. Digestion buffer was neutralized with 5 mL heat-inactivated FBS, washed with PBS, and filtered through 70 μ m filters. Single cell suspensions were pelleted at 1500 rpm with slow deceleration, and transferred to 96-well round-bottom plates for flow cytometric staining. Spleen samples were mashed through 70 μ m filters, collected in RPMI 1640 supplemented with 1% heat-inactivated FBS and pelleted. Red blood cells were lysed with ACK buffer for 2 min before cell suspension neutralization with PBS, pelleted for plating and transferred to 96-well round-bottom plates for flow cytometric staining. Prior to surface staining, cell pellets were resuspended in Live/Dead dye (Ghost Dye Red 780, Tonbo Biosciences or Zombie Aqua Fixable Viability Dye, BioLegend) diluted 1:1000 in PBS on ice for 20 minutes in the dark. Surface staining was performed on cells in PBS with 1% heat-inactivated FBS on ice for 30 min in the dark. Cell pellets were fixed overnight in 1X fixation buffer (eBioscience), prior to permeabilization and intracellular staining for 1 hour in the dark at room temperature. Full antibody and tetramer information in [Table S4](#). We thank the NIH Tetramer Core Facility (contract number 75N93020D00005) for providing H-2Kb_SIIIFEKL (OVA257-264), H-2Kb_VGFNFRFL (mLAMA4), and H-2Kb_ITYTWRFL (mALG8) tetramers.

Flow cytometry of human PDAC

All human studies were performed using de-identified human biospecimens and studies were approved by the Massachusetts General Brigham Institutional Review Board and conducted according to the principles expressed in the Declaration of Helsinki. The study was in strict compliance with all institutional ethical regulations. All tumor samples were surgically resected primary pancreatic ductal adenocarcinomas and were de-identified prior to researcher processing. Briefly, freshly resected human PDAC specimens were transferred in RPMI 1640 on ice to the laboratory. Pancreas tumors were finely minced with scissors in MACS C tubes, and processed as described above for murine PDAC. Healthy peripheral blood (human PBMCs) from IRB-consented healthy individuals was purchased from StemCell. Antibody information in [Table S4](#). As all biospecimens were de-identified, information about age and sex is unavailable. PD-1 staining was omitted during processing of one PDAC biospecimen, so this sample was not included into co-expression analyses with PD-1, but was included in other analyses.

For all flow cytometry experiments, samples were acquired on BD LSR II or LSR Fortessa machines, cell sorting was performed on a BD Aria IIIu. UltraComp eBeads (eBioscience) or single-fluorophore expressing organoids were used for compensation. For murine *in vivo* experiments, endogenous CD44^{lo}CD8⁺ T cells and healthy spleens were used for negative controls and gating. For human experiments, healthy peripheral blood was used as negative controls and gating. For *in vitro* experiments, unstained controls and fluorescence minus one were used for negative controls and gating. Specimens with fewer than 100 live CD8s (mouse) or 200 live CD8s (human) were not considered for further immunophenotyping. FACS data was analyzed using Flowjo v10 software (BD Biosciences).

Immunohistochemistry and pathology review

Tissues were preserved in zinc formalin fixative for 16–24 hours within 1 hour of necropsy, transferred to 70% EtOH, and processed for paraffin embedding. For immunohistochemical staining, slides were blocked using Endogenous Peroxidase Block (Dako) or Bloxall Endogenous Peroxidase and Alkaline Phosphatase Block (Vector Labs) according to manufacturer instructions, followed by incubation with horse serum (Vector Labs) for 1 hour at room temperature. Slides were incubated with primary antibody overnight at 4°C. Details on epitope retrieval and primary antibodies can be found in [Table S4](#). The following day, slides were incubated with the appropriate anti-species HRP-conjugated secondary antibody (Vector Labs) for 30 minutes at room temperature. Slides were developed with DAB Peroxidase Substrate Kit (Vector Labs) unless otherwise indicated.

For CD8 and CD4 co-staining, slides were blocked with Bloxall and normal horse serum as above. Slides were incubated with primary rabbit anti-CD8 antibody (Abcam EPR21769, 1:1000) overnight at 4°C and with secondary Alkaline phosphatase anti-Rabbit IgG for 30 minutes at room temperature. Slides were then developed with Vector Black Alkaline phosphatase substrate (Vector Labs) and blocked again with Bloxall and horse serum. Slides were incubated with primary rabbit anti-CD4 (Abcam EPR19514, 1:400) for 3 hours at room temperature and secondary HRP conjugated anti-Rabbit antibody for 30 minutes. Slides were developed with HRP Vina Green Chromogen (Biocare Medical). All murine histologic diagnoses were confirmed with a pathologist (R.T.B.) specialized in rodent pathology.

For CD155 IHC in human tissues, a pancreatic adenocarcinoma tissue microarray (PA1002b) was purchased from Biomax. Anti-CD155 (EPR22672-151) (ab267788; Abcam) was used at 1:500 dilution (final 1.01 μ g/mL) following HIER with Tris-EDTA pH 9 (ab93684; Abcam). Slides were reviewed and scored by a board-certified pathologist (G.E.) with membranous staining on tumor cells scored based on intensity of staining as 0, 1+, 2+, 3+. Cores that were missing from TMA (n=1), lacked tumor epithelium (n=2), or that were found on pathologic review to likely represent pancreatic neuroendocrine tumor (n=1) were excluded from further analysis. H-scores were obtained by the formula: (3*percentage of strongly staining cells [3⁺]) + (2* percentage of moderately staining cells [2⁺]) + (1*percentage of weakly staining cells [1⁺]) as previously described ([Hirsch et al., 2003](#)). Histopathologic and immunohistochemical analyses were performed using QuPath ([Bankhead et al., 2017](#)).

Nanostring GeoMx digital spatial profiling

FFPE tissues were sectioned and processed according to NanoString GeoMx DSP guidelines. Briefly, 5 μm sections were placed on SuperFrost Plus slides. Details on epitope retrieval and primary antibodies can be found in [Table S4](#). Tissue morphology markers in the mouse solid tumor morphology kit included PanCK and CD45, and a custom CD8a stain was additionally included. Protein probe sets included the Immune Cell Profiling Core, IO Drug Target Module, Immune Activation Status Module, and Immune Cell Typing Module. Geometric areas of interest (AOIs) were annotated for therapy response and spatial localization as tumor center, tumor periphery, CD8_high, CD8_low, responder, non-responder. The GeoMx platform was similarly used for mIHC with the antibodies detailed above.

Data QC, normalization, and feature-based selection

Raw expression data were checked for quality and ERCC-normalized prior to statistical analyses. First, raw expression data were checked for hybridization quality by calculating hybridization factors (ERCC normalization factors). A hybridization factor for a given sample (AOI) was defined as the mean of all HYB-POS values in the dataset divided by that sample's HYB-POS value. Any samples with a hybridization factor of 10 or more were discarded. ERCC normalization was subsequently performed by multiplying all proteins for a given sample by its respective hybridization factor.

Three isotype control molecules were measured for each sample: Rb IgG, Rt IgG2a, and Rt IgG2b. Rt IgG2b, was removed as it showed a reduced correlation with other IgG controls and a greater root mean squared error with the other two (RMSE = 0.29 and 0.30, respectively). Samples were normalized by calculating a normalization factor based on the geometric mean of each sample's Rb IgG and Rt IgG2a expression values. The mean of these geometric means was divided by a given sample's geometric mean value to generate that sample's specific normalization factor. Normalization was then performed by multiplying all proteins for a given sample by its respective normalization factor.

Forty proteins—including S6, Histone H3, GAPDH housekeeping proteins—were measured. These proteins were filtered based on signal to noise ratio (SNR), as calculated by the ERCC-normalized expression for that feature divided by that sample's geometric mean of Rb IgG and Rt IgG2a. A feature was retained if the median SNR value was greater than one. One protein, CD163, had a median SNR of 0.29, but was kept for downstream analysis given prior reports of M2 macrophage polarization in immune evasion.

Statistical analyses

Hierarchical clustering was performed on the Z-scores of the log₂ transformed normalized data using the R package pheatmap ([Ihaka and Gentleman, 1996](#); [Kolde, 2019](#)). Differential expression analysis was performed between CD8⁻ compartments (2 mice; 11 AOIs) and CD8⁺ compartments (3 mice; 25 AOIs). To account for multiple samples taken within a given mouse, a mixed effect model implemented from the R package lmerTest ([Kuznetsova et al., 2017](#)). For a given protein, its log₂ transformed expression was used as the dependent variable, CD8 status (CD8⁻, CD8⁺) was used as a fixed effect and mouse ID was used as the random effect (with random intercept). Satterthwaite's approximation ([Kuznetsova et al., 2017](#)) was used to estimate the degrees of freedom for p-value calculation. Any protein with a singular fitted model were discarded. To account for multiple hypothesis testing, the Benjamini-Hochberg FDR was used ([Benjamini and Hochberg, 1995](#)).

Single-cell RNA sequencing

Sorted cells were washed three times in 1x PBS (calcium and magnesium free) containing 0.04% w/v BSA, and then quantified and titrated to a final concentration of approximately 300 cells/ μL . Using the Chromium Single Cell 3' Solution (v3) according to manufacturer's instructions (10x Genomics), approximately 2000-5000 cells were partitioned into Gel Beads in Emulsion (GEMs) with cell lysis and barcoded reverse transcription of mRNA into cDNA, followed by amplification, enzymatic fragmentation and 5' adaptor and sample index attachment. The recovery rate was ~800 cells per sample after filtering for quality control. Sample libraries were sequenced on the HiSeq X Version 2.5 (Illumina) with the following read configuration: Read1 28 cycles, Read2 96 cycles, Index read 8 cycles.

Single-cell RNA sequencing analysis

Data processing, cell clustering, and differential expression analysis

Raw sequencing data was processed using Cell Ranger, version 3.0.2, and sequencing reads were aligned to the mm10 reference mouse transcriptome (version 3.0.0). After processing, Cell Ranger reported 789 cell-associated barcodes and detected 31,053 genes. These data were loaded into R, version 4.0.3, and further processed with Seurat, version 3.2.2 ([Butler et al., 2018](#)). Genes not expressed in any cells were filtered out. After this, low-quality cells containing more than 10% of reads matching the mitochondrial genome were excluded. Cells with less than 100 detected genes were then filtered. Finally, cells lacking expression of either Cd8a or Cd3e were removed, and cells exceeding the 97th percentile (4,065) for number of detected genes were excluded to remove probable doublets. The resulting matrix used for downstream analyses was defined by 447 cells and 15,065 genes. Data normalization and scaling, variable feature selection, cell clustering, and differential gene expression analysis was performed using Seurat. Data were normalized by total expression per cell and scaled using a factor of 10,000 and log transformed (natural scale). The top 2,000 variable genes were selected using Seurat's default "vst" method. The expression of these genes was then scaled and centered, and these genes were then used for all downstream analysis. Principal component analysis (PCA) was then performed for dimensionality reduction, and the first 30 principal components were selected with the elbow method as a heuristic.

A k-nearest neighbor graph (KNN, k=20) was constructed in PCA space using the top 30 principal components. Four clusters were detected using the Louvain method of community detection (default parameters and resolution = 0.69) ([De Meo et al., 2011](#)). Data

was visualized using the Uniform Manifold Approximation and Projection (UMAP) algorithm implemented in Seurat (Becht et al., 2019; McInnes et al., 2018). Default parameters were used, with the following exceptions: the method parameter (“umap-learn”) and the metric parameter (“correlation”). Differential gene expression (min logfc = 0.4; min pct = 20) between clusters was assessed using the default Wilcoxon Rank Sum test.

Gene module analysis

Seurat’s AddModuleScore function (control parameter = 8) was used to calculate gene module scores for all cells. For this analysis, gene sets were derived from previously published gene modules (Table S2). For datasets providing human gene modules, a custom R script was generated to retrieve corresponding mouse orthologs from Ensembl with the biomaRt package (version 2.42.0) (Durink et al., 2005, 2009).

To derive *de novo* gene modules from our scRNA-seq dataset, the Pathway and Gene Set Overdispersion Analysis (PAGODA) (Fan et al., 2016) framework from the SCDE package (version 2.14.0) was used. The analysis was performed starting with the raw counts for the same 447 cells that remained after filtering in the previous analysis. The knn error model was fit using min.count.threshold = 2 and $k = \text{ncol}(\text{cd}/4)$, where “cd” represented the matrix after clean.counts was performed with default parameters. Gene expression magnitudes were then normalized with trim = $3/\text{ncol}(\text{cd})$ and max.adj.var=5. *De novo* gene modules were then determined using trim = $7.1/\text{ncol}(\text{varinfo}\$mat)$ and n.clusters = 50 and otherwise default parameters for the pagoda.gene.clusters function. The top three *de novo* gene sets (modules 30, 36, and 45) with the highest over-dispersion Z score (adjusted for multiple hypotheses) that best distinguished the cellular subpopulations defined by SCDE were selected, and all cells were scored for these modules in Seurat as described above.

QUANTIFICATION AND STATISTICAL ANALYSIS

Statistical analyses

All graphs and statistical analyses were generated with GraphPad Prism 9 or in the R statistical programming language (R-project.org) as described above. The following statistical tests were used in this study: (1) two-sided Mann-Whitney test, (2) two-sided t-test with Welch’s correction, (3) two-sided Kolmogorov-Smirnov (KS), (4) linear mixed effect model with Benjamini-Hochberg FDR. Figure legends specify the statistical tests used, exact value of n, definition of center, and dispersion and precision measures. Figure legends also specify how significance was defined.

Clinical data analysis

RNA-seq gene expression profiles (normalized counts) from primary tumors of lung adenocarcinoma (LUAD) (Collisson et al., 2014), pancreatic ductal adenocarcinoma (PAAD) (Cancer Genome Atlas Research Network, 2017), and colorectal adenocarcinoma (COAD) (Muzny et al., 2012) patients were obtained from The Cancer Genome Atlas (TCGA, gdac.broadinstitute.org). Patients within each cohort were limited to those included in the TCGA Pan-Cancer Atlas study (Hoadley et al., 2018) for which mutational profiles were available on cBioPortal (cBioPortal for Cancer Genomics, cbioportal.org) (Gao et al., 2013). Patients in the PAAD cohort were further limited to those included in the TCGA PAAD study (Cancer Genome Atlas Research Network, 2017). Within each cancer type, patients were grouped according to *KRAS* and *TP53* mutational status, as retrieved from cBioPortal (KP = alterations in *KRAS* and in *TP53*; nonKP = the remainder of the cohort). Standardized expression levels of *PVR* were illustrated across KP and nonKP patient groups using Empirical Cumulative Distribution Function (ECDF) plots where significance was assessed using a Kolmogorov-Smirnov test.

Neoepitope prediction

In the TCGA cohort, 148 PDAC patients were analyzed (of 150). One patient lacking a normal BAM file was excluded, and another patient was also excluded due to hypermutation (Cancer Genome Atlas Research Network, 2017). In the DFCI-PancSeq cohort, 57 patients with (1) annotated mutations, (2) both WES and RNA-seq data, and (3) sufficient tumor purity (Aguirre et al., 2018) were analyzed. Binary Alignment Map (BAM) files were obtained for PancSeq (aligned to GRCh37) and for TCGA (aligned to GRCh38). Thus, GRCh37 was used as the reference genome for the PancSeq cohort in all downstream analyses, and GRCh38 was used for the TCGA cohort.

HLA typing was performed using two programs and with both RNA-seq and WES data to assess robustness of HLA allele calls. HLA alleles for classical genes (HLA-A, -B, and C) were called using the HLA genotyping algorithm, OptiType, version 1.3.1 (Szolek et al., 2014), as well as seq2HLA, version 2.3 (Boegel et al., 2012), which was also used to identify alleles for HLA-E. Tumor and normal WES BAM files were used to create inputs to OptiType, which outperforms peer programs in WES-based HLA-typing (Bauer et al., 2018), and RNA-Sequencing BAMs were used to create inputs to seq2HLA. WES BAMs were filtered to retain only reads mapping to the HLA region (6:28477897-33448354 in GRCh37; chr6:28510120-33480577 in GRCh38) with the genomics software suite, Samtools, version 1.10 (Li et al., 2009). The BAMs were then converted to FASTQ format, and then filtered with the genome mapping tool, RazerS 3, version 3.5.8 (Weese et al., 2012), as recommended in the OptiType documentation. RNA-Seq BAMs were sorted, converted to FASTQ format, and compressed before being used as inputs to seq2HLA. Both programs were run with default parameters.

A custom python script was then employed to evaluate concordance between (1) normal and tumor HLA allele calls from WES and (2) seq2HLA and OptiType calls. Only 4/342 alleles (0.58%) in the PancSeq cohort and only 2/888 (0.23%) alleles in the TCGA cohort were called differently between tumor and normal WES-based calls. Given the consistency of OptiType calls for tumor and normal WES data, the OptiType allele was accepted as the final call to resolve discrepancies between OptiType and Seq2HLA.

Mutation Annotation Format (MAF) files were obtained for patients in both datasets and converted to Variant Call Format (VCF) files. VCF files were filtered to only retain single nucleotide variants (SNVs). Only PASS variants were available in the PancSeq MAF file and were thus not filtered further (Aguirre et al., 2018). Mutations in the TCGA cohort included non-PASS variants, which were all filtered in this cohort with the exception of some non-PASS mutations in known PDAC-associated genes that had been marked as either `panel_of_normals`, `clustered_events`, or `homologous_mapping_event` in the TCGA MAF file. For these cases, genes that had variants marked as non-PASS more than twice by at least one of these filters were reconsidered. The following genes with a known association with PDAC based on a literature search were retained: *KRAS*, *TP53*, *GNAS*, *RNF43*, *PLEC*, *FLG*, *AHNAK*, *APOB*, *CSMD1*, *PLXNA1*, *MCM6*, *MKI67*, and *SIPA1*. This step was intended to reduce false negatives, and in the case of *KRAS*, this step retrieved 30 variants at residue position 12, a site known to confer oncogenic properties when mutated.

Indel variants were called using the variant callers, Strelka2, version 2.9.2 (Kim et al., 2018), and Scalpel, version 0.5.4 (Narzisi et al., 2014). The structural variant and indel caller, Manta, version 1.6.0 (Chen et al., 2016), was run prior to Strelka2 and these results were incorporated into the `indelCandidates` parameter for Strelka2. Scalpel was run with default parameters, with a bed file derived from the CGHub bitbucket account (<https://cghub.ucsc.edu>; `whole_exome_agilent_1.1_refseq_plus_3_boosters.targetIntervals.bed`). For the PancSeq cohort, the unmodified first 3 columns of this file were used. For the TCGA cohort, the coordinates in this file were converted to GRCh38 coordinates using the LiftOver tool from the UCSC genome browser (Haeussler et al., 2019). Scalpel failed to call variants for 13/148 TCGA patients due to excessive read buildup at some loci. To enable variant calling with Scalpel for these patients, the Picard tools' `DownsampleSam` function (<http://broadinstitute.github.io/picard/>) was employed to randomly downsample reads in the tumor BAM files of these patients by decrements of 10%, starting at 50%. This was done until Scalpel successfully called variants for each patient. Ten patients succeeded at 50%, two at 40%, and one at 30%.

To reduce the contribution of caller-specific biases and hence the indel false positive rate, only those indels that were called and marked as PASS by both Scalpel and Strelka2 were retained. Variant call format (VCF) files containing the intersection of PASSed variants from Strelka2 and Scalpel were generated with a custom batch script, and variant allele frequencies were calculated using statistics output by Strelka2. These indel VCF files were then merged with the corresponding SNV VCF files for each patient using the `vcf-shuffle-cols` and `vcf-concat` functions from VCFtools, version 0.1.13 (Danecek et al., 2011).

Variant consequence was then annotated using the Ensembl Variant Effect Predictor (VEP), version 99 (McLaren et al., 2016). The corresponding VEP cache for both GRCh37 and GRCh38 was downloaded and used to run the software offline. VEP was run using the `Wildtype` and `Downstream` plugins to annotate the effects of indels. The following parameters were employed: `-symbol`, `-terms=SO`, `-cache`, `-offline`, `-transcript_version`, `-pick`. The `-pick` parameter was reordered from the default to report the transcript with the most extreme consequence for each variant: `rank`, `canonical`, `appris`, `tsl`, `biotype`, `ccds`, `length`, `mane`.

Neoepitopes were predicted with the HLA allele calls and variant effect predictions using the antigen prediction toolkit, pVACtools, version 1.5.7 (Hundal et al., 2020). For each mutation, mutant peptides were generated for lengths of 8-, 9-, 10-, and 11- amino acids, the spectrum of peptide lengths known to bind to MHC class I. MHC:peptide binding affinity was predicted for all peptide:MHC allele pairs with NetMHC-4.0, NetMHCpan-4.0, SMM (version 1.0), and SMMPMBEC (version 1.0) (Andreatta and Nielsen, 2016; Jurtz et al., 2017; Li et al., 2009; Peters and Sette, 2005), and the median value across all affinity predictions was taken as a final, composite measure of binding affinity.

After predictions were made by pVACtools, candidate neoepitopes from all patients were merged into a single matrix and filtered using a custom python script and the following criteria (based on parameters output by pVACtools): median peptide:MHC binding affinity < 500 nM, tumor DNA depth ≥ 5 , tumor DNA variant allele frequency ≥ 0.07 , `cysteine_count` ≤ 1 , and a median `wildtype:-mutant peptide binding affinity fold-change` ≥ 1 . After filtering, the total number of remaining candidates was summed per patient and predicted neoepitopes were classified in the following binding affinity ranges: 50-500 nM, 10-50 nM, and 0-10 nM. Neoepitopes were also classified as nonbinders-to-binders (WT nM > 1000 and MT < 500 nM) and nonbinders-to-strong binders (WT nM > 1000 nM and MT < 50 nM). All frameshift-derived neoepitopes with a binding affinity < 500 nM and no corresponding wildtype peptide sequence were also classified as nonbinders-to-binders.

scRNA-seq analysis of human PDAC

Human PDAC scRNA-Seq data (Peng et al., 2019) was downloaded from the Genome Sequencing Archive (accession: CRA001160). A count matrix of 41,987 pre-processed cells was prepared from these data and used to create a Seurat object. Genes expressed in less than 10 cells were filtered out. Data normalization, scaling, variable feature selection, and principal components analysis were then carried out as described for the murine scRNA-Seq analysis. The first 15 principal components were used for the construction of the k-nearest neighbor graph and the UMAP plot (metric parameter = Euclidean). Clusters were then assigned using the Louvain method with a resolution of 1.

For the T cell subset analysis, cells were selected out from the larger dataset based on expression of *CD8A* and either *CD3E*, *CD3D*, or *CD3G*. Cells expressing both *CD3* and *CD4* were selected in the same way, using *CD4* expression instead of *CD8A*. Genes detected in less than 5 cells were then excluded from the 2 subset matrices individually. These two subsets were then merged to form a new matrix consisting of 3,409 cells and 18,349 genes. These data were then processed as described for the whole dataset,

revealing batch effects that caused cells to separate in UMAP space according to their patient of origin. To construct a batch-corrected UMAP, Seurat's integration workflow was performed (Stuart et al., 2019). Cells were split into individual matrices according to their patient of origin, and matrices corresponding to patients possessing less than 50 cells were excluded to accommodate a *k*.filter parameter of 50 for the integration anchor identification step. 3,320 cells remained after this step. Pearson residuals were then utilized for data normalization and scaling, as implemented in the SCTransform function (Hafemeister and Satija, 2019). 3,000 integration features were then selected and incorporated as input in the integration anchors identification step. Principal components analysis, *k*-nearest neighbor graph and UMAP construction (PC dimensions = 14), and cluster annotation (resolution = 0.8) were then performed as described before. For feature plotting and differential gene expression analysis, the UMI count matrix of these cells was separately normalized and scaled as described for the whole dataset. Differential gene expression between clusters was then assessed with the Wilcoxon Rank Sum test. Genuine T cell clusters (0, 1, 8, and 9) were then distinguished by differentially higher expression of *CD3* and/or *CD4* and *CD8A* and by a differentially reduced or complete lack of expression of antigen-presenting cell markers that defined other clusters. To plot murine TIL-derived PAGODA modules on human data, the custom R script described for module analysis of murine scRNA-Seq was employed to retrieve human orthologs of each gene comprising each PAGODA module. The human orthologs were then used to compute module scores with Seurat's AddModuleScore function (control parameter = 8).